Involvement of PHOSPHATE TRANSPORTER TRAFFIC FACILITATOR1 in COPII assembly by interacting with SAR1 GTPase

Hui-Fang Lung[a], Jia-Dong Chu[a], Tzu-Yin Liu[a, b,1]

[a]Institute of Bioinformatics and Structural Biology, College of Life Sciences and Medicine, National Tsing Hua University, Hsinchu 30013, Taiwan.

[b]Department of Life Science, College of Life Sciences and Medicine, National Tsing Hua University, Hsinchu 30013, Taiwan.

[1]Address correspondence to tzliu@life.nthu.edu.tw

Institute of Bioinformatics and Structural Biology, College of Life Sciences and Medicine, National Tsing Hua University, Hsinchu 30013, Taiwan

Tel: +886 3 574-2096, Fax: +886 3 571-5934

Corresponding author:

Tzu-Yin Liu

Email: tzliu@life.nthu.edu.tw

Abstract

Inorganic phosphate (Pi) uptake and translocation are crucial for plant growth and development, relying on plasma membrane targeting of PHOSPHATE TRANSPORTER1 (PHT1) transporters. The plant-specific endoplasmic reticulum (ER)-resident PHOSPHATE TRANSPORTER TRAFFIC FACILITATOR1 (PHF1) is structurally related to SEC12, which initiates the coat protein complex II (COPII) assembly as a guanine nucleotide exchange factor (GEF) by activating the small GTPase SAR1. In contrast, PHF1 loses the conserved catalytic residues critical for GEF activity and specifically assists the ER exit of the PHT1 transporters. However, the underlying molecular mechanism remains unknown. In this study, we showed that overexpression of *Arabidopsis thaliana* PHT1;1 (*At*PHT1;1) in the tobacco transient expression system caused a portion of *At*PHF1 distribution into *At*SAR1b- and *At*SEC24a-labeled ER exit sites. We demonstrated that *At*PHF1 interacts with *At*SAR1b and *At*SAR1c based on the tripartite split-GFP association in agro-infiltrated tobacco leaves and verified this interaction using miniTurbo-based proximity labeling. We also confirmed its physiological relevance by co-immunoprecipitation of the endogenous *At*PHF1 with *At*SAR1c-GFP in *Arabidopsis* transgenic lines. Importantly, *At*PHF1 preferentially interacts with the GDP-locked *At*SAR1. Therefore, we propose that PHF1 interacts with the SAR1 GTPase to participate in the early step of COPII recruitment for the ER export of PHT1 transporters.

Keywords: PHOSPHATE TRANSPORTER1, PHOSPHATE TRANSPORTER TRAFFIC FACILITATOR1, coat protein complex II (COPII), ER exit sites (ERES)

Introduction

As sessile organisms, plants adjust the protein and lipid composition of the plasma membrane (PM) to sense and adapt to the ever-changing environment. Such dynamic cellular processes heavily rely on the modulation of the endomembrane trafficking system (Wang et al., 2020), including the coat protein complex II (COPII)-mediated endoplasmic reticulum (ER)-to-Golgi transport pathway. Although the core COPII machinery, composed of five cytosolic factors, SAR1, SEC23, SEC24, SEC13, and SEC31, is conserved throughout all eukaryotes, the mechanisms underlying COPII recruitment and assembly are most extensively studied in the budding yeast *Saccharomyces cerevisiae* (Barlowe and Miller, 2013). In this model organism, the COPII-related components are encoded by single genes and recruited sequentially to the ER exit sites (ERES) (Kurokawa and Nakano, 2019). The SAR1 GTPase is activated upon the exchange of GDP to GTP by the guanine nucleotide exchange factor (GEF) SEC12, exposing its amphipathic N-terminal helix to be inserted into the ER membrane (d'Enfert, 1991; Paul et al., 2023). SAR1 then interacts directly with SEC23, inducing the formation of the inner coat SEC23–SEC24 complex, which in turn recruits the outer coat SEC13–SEC31 complex (Bi, 2002; Stagg et al., 2006). In addition, SEC16, an initial factor assembled at the ERES, serves as a scaffold protein by concentrating SEC12 and GTP-bound active SAR1 in proximity (Supek et al., 2002; Montegna et al., 2012). By comparison, the plant COPII subunit paralogs are encoded by multi-gene families and outnumber those in other organisms (Chung et al., 2016). Multiple COPII paralogues allow the diversity of COPII transport carriers to adapt to various developmental and stress-related cues (Chung et al., 2016; Wang et al., 2020). For instance, the phytohormone abscisic acid triggered the formation of *Arabidopsis thaliana* SAR1a (*At*SAR1a)-dependent COPII vesicles that carry osmotic stress-related carriers (Li, 2021). The *At*SAR1a-*At*SEC23a pairing was also shown to mediate the ER export of the ER-associated transcription factor bZIP28, which is upregulated in response to ER stress (Zeng et al., 2015).

75 By contrast, the mechanism by which the COPII machinery regulates protein ER export to cope
76 with nutrient deficiency remains unknown.
77 Inorganic phosphate (Pi) is an essential macronutrient for plant growth. Due to its poor
78 solubility and mobility in soil, Pi bioavailability is limited, thus causing plants to face Pi
79 deficiency (Shen, 2011). Under Pi-limited conditions, plants enhance the external Pi uptake as
80 well as the recycling and remobilization of internal Pi, which involves the upregulation of the
81 *PHOSPHATE TRANSPORTER1* (*PHT1*) gene family at the transcript and post-transcriptional
82 level (Nussaume et al., 2011). While most *PHT1* genes are upregulated by Pi deprivation, the
83 newly synthesized PHT1 proteins (PHT1s) must exit the ER for the PM targeting. Similar to
84 the inhibitory effect of SEC12 overexpression on the ER export of the Golgi transmembrane
85 protein ERD2 in tobacco leaves (Hanton et al., 2007), the overexpression of SEC12 impaired
86 the PM targeting of *At*PHT1;2 (Bayle et al., 2011). Thus, the ER-to-Golgi transport of PHT1s
87 is dependent on efficient COPII assembly. Interestingly, the plant-specific SEC12-related
88 protein PHOSPHATE TRANSPORTER TRAFFIC FACILITATOR1 (PHF1) was identified to
89 facilitate the ER exit of *At*PHT1s (González et al., 2005; Bayle et al., 2011). Despite sharing
90 the sequence similarity with SEC12, *At*PHF1 lost the conserved catalytic residues critical for
91 GEF activity and failed to rescue the growth defect of the yeast *sec12* mutant (González et al.,
92 2005). Instead, the *Arabidopsis* loss-of-function *phf1* mutant showed decreased cellular Pi
93 content and impaired PM targeting of *At*PHT1;1 (González et al., 2005). As the role of PHF1
94 in assisting the ER exit of PHT1s resembles that of the yeast Pho86p in the ER exit of Pho84p,
95 the yeast homolog of PHT1s (Lau, 2000), PHF1 may functionally diverge from SEC12
96 (González et al., 2005).
97 The transient protein expression using tobacco leaves is a well-established plant system to study
98 the dynamic organization of COPII proteins at the ERES (daSilva et al., 2004; Hanton et al.,
99 2009). In this system, the ERES formation can be monitored by the subcellular distribution of
100 fluorescent protein-tagged COPII components changing from cytosolic patterns into punctate

101 structures (daSilva et al., 2004; Hanton et al., 2007; Hanton et al., 2008; Hanton et al., 2009).
102 Overexpression of COPII-dependent membrane cargoes enhanced the recruitment of YFP-
103 *At*SEC24a to the ERES as well as induced the *de novo* formation of ERES (Hanton et al., 2007).
104 Likewise, *At*PHT1;2-CFP overexpression resulted in the recruitment of YFP-*At*SEC24a to
105 ERES puncta, reinforcing that the ER export of *At*PHT1s is COPII-dependent (Bayle et al.,
106 2011). Although the ER-resident *At*PHF1 failed to co-localize with *At*SEC24a, thus leading to
107 the conclusion that *At*PHF1 is not involved in COPII recruitment (Bayle et al., 2011), it remains
108 unclear whether PHF1 participates in cargo recognition or the selective packaging of PHT1
109 transporters into COPII vesicles.
110 Since PHF1 shares sequence similarity with SEC12 yet exhibits a distinct function, we
111 speculated that PHF1 may engage in the COPII-dependent ER export of PHT1s on a molecular
112 basis different from that of SEC12. To explore this hypothesis, we aimed to investigate whether
113 *At*PHT1;1 overexpression can induce the distribution of *At*PHF1 into ERES puncta and whether
114 *At*PHF1 can interact with COPII-related components. Using agro-infiltrated tobacco leaves, we
115 showed that overexpression of *At*PHT1;1 triggered a portion of *At*PHF1 distribution into
116 punctate structures that partially co-localized with *At*SAR1b and *At*SEC24a. Furthermore,
117 based on the tripartite split-GFP association, *At*PHF1 interacted with *At*SAR1b and *At*SAR1c,
118 but not with *At*SEC24a or other COPII-related components. Consistently, we verified the
119 interaction of *At*PHF1 and *At*SAR1b by the proximity labeling in the transient tobacco system
120 and demonstrated that the endogenous *At*PHF1 and *At*PHT1;1/2/3 were co-immunoprecipitated
121 with *At*SAR1c-GFP in *Arabidopsis* transgenic lines. More importantly, we showed that, like
122 *At*SEC12, *At*PHF1 preferentially interacted with the GDP-locked inactive form of *At*SAR1b.
123 Our results unveiled that *At*PHF1 may act as an early regulator of COPII assembly for the ER
124 export of *At*PHT1s through interacting with *At*SAR1 proteins (*At*SAR1s).
125
126 **Results**

127 **Overexpression of *At*PHT1;1 triggers partial distribution of *At*PHF1 into ERES-**
128 **associated punctate structures**
129 Both the mammalian and plant SEC12 proteins are dispersed throughout the ER (Weissman et
130 al., 2001; Bayle et al., 2011). However, the mammalian SEC12 can be concentrated at the ERES
131 by the collagen cargo receptor component cTAGE5 for the ER export of collagen (Saito et al.,
132 2014). We thus wondered whether the SEC12-related *At*PHF1, which was reported to distribute
133 evenly across the ER (González et al., 2005; Bayle et al., 2011), can be induced to concentrate
134 at ERES when the ER export of *At*PHT1;1 is highly demanded. When expressed alone in agro-
135 infiltrated tobacco leaves, *At*PHF1-GFP showed a reticular ER pattern, while a portion of
136 *At*PHF1-GFP displayed punctate-like structures when the split-GFP tagged *At*PHT1;1
137 (*At*PHT1;1-S11) was co-expressed (**Fig. 1A**). By contrast, the co-expression of *At*PHF1-GFP
138 with the sugar transporter *At*STP1-S11 barely changed the distribution of *At*PHF1-GFP (**Fig.**
139 **1A**). Statistical analysis further suggested that the overexpression of *At*PHT1;1-S11 but not of
140 *At*STP1-S11 significantly triggered the partial distribution of *At*PHF1-GFP into punctate
141 structures (**Fig. 1B**).
142 To ensure that the formation of *At*PHF1 puncta triggered by *At*PHT1;1 overexpression is not
143 due to the ER morphological changes, we examined the ER organization using the ER lumen
144 marker mCherry-HDEL. The overexpression of *At*PHT1;1-S11 did not change the overall ER
145 morphology labeled by the mCherry-HDEL marker (**Supplementary Fig. S1**), but we
146 occasionally observed the formation of mCherry-HDEL- or *At*PHF1-GFP-labeled puncta upon
147 the overexpression of *At*PHT1;1 (**Fig. 1C**). We then classified the *At*PHT1;1-induced puncta
148 into three groups for quantification: the distinct *At*PHF1-labeled puncta that did not overlap
149 with the mCherry-HDEL puncta, the distinct mCherry-HDEL-labeled puncta that did not
150 overlap with the *At*PHF1-labeled puncta, and the overlapping puncta. Statistical analyses
151 indicated that the distinct *At*PHF1-labeled puncta predominated over the overlapping puncta
152 (**Fig. 1D**; detailed analysis of individual experiment in **Supplementary Fig. S2A**), suggesting

153 that the majority of the *At*PHT1;1 overexpression-induced *At*PHF1 puncta represented a
154 compartment different from the mCherry-HDEL-labeled puncta.
155 In the tobacco transient expression system, the co-expression of membrane cargoes recruited
156 the COPII components, such as *At*SAR1 and *At*SEC24, to concentrate at the punctate ERES
157 (Hanton et al., 2007; Hanton et al., 2008). Intriguingly, the populations of *At*PHF1 puncta upon
158 *At*PHT1;1 overexpression displayed a size with a median of 0.66–0.77 μm (**Supplementary**
159 **Fig. S2B**), which is comparable to the previously reported size of ERES puncta with a range of
160 0.15–0.8 μm across various organisms (Bannykh, 1996; Yang et al., 2005; Zeuschner et al.,
161 2006; Takagi et al., 2020; Weigel et al., 2021). To address whether the punctate structures of
162 *At*PHF1-GFP induced by the overexpression of *At*PHT1;1 might represent ERES, we selected
163 *At*SAR1b as a COPII marker to co-localize with *At*PHF1-mCherry. This is because *AtSAR1b* is
164 the most highly expressed *AtSAR1* gene in roots and is upregulated in response to Pi deprivation
165 (Liu et al., 2016) (**Supplementary Fig. S3**). In addition, the previous proteomic analysis of the
166 Pi overaccumulator *pho2* root has revealed the co-induction of *At*SAR1b and *At*PHT1s (Huang
167 et al., 2013), implying an increased demand for *At*SAR1b to promote the ER-to-Golgi traffic of
168 *At*PHT1s. Considering that the N-terminal tail of SAR1 is inserted into the ER membranes upon
169 activation (d'Enfert, 1991; Paul et al., 2023), we fused the S11 tag to the C terminus of *At*SAR1b
170 to prevent steric hindrance. In tobacco epidermal cells, *At*SAR1b-S11 exhibited both a diffuse
171 cytosolic distribution and an ER membrane-associated punctate pattern, similar to the
172 previously reported results (Yang et al., 2005; Hanton et al., 2008) (**Supplementary Fig. S4A**).
173 *At*SEC24a is involved in cargo selection for COPII vesicles and is also widely used as a reliable
174 ERES marker (Miller, 2002; Hanton et al., 2007); therefore, we generated a construct
175 expressing *At*SEC24a-S11 for co-localization with *At*PHF1-mCherry as well. The subcellular
176 localizations of *At*SEC24a-S11 displayed the cytosolic and punctate patterns (**Supplementary**
177 **Fig. S4A**). *At*PHT1;1 overexpression induced the formation of *At*PHF1-mCherry punctate
178 structures that colocalized with the *At*SAR1b- and *At*SEC24a-labeled ERES (**Fig. 2A** and **2B**).

179 Statistical analyses further suggested that the majority of *At*PHF1-mCherry puncta overlapped
180 with these two ERES markers (**Fig. 2C**; detailed analysis of individual experiment in
181 **Supplementary Fig. S5A** and **S5B**). The size of the overlapping puncta was also comparable
182 to that of the distinct *At*SAR1b- and *At*SEC24a-labeled puncta, with a median of 0.67–0.81 μm
183 (**Supplementary Fig. S5C** and **S5D**). The co-localization analysis further indicated a better
184 spatial co-occurrence of *At*PHF1-mCherry puncta with *At*SAR1b than with *At*SEC24a, as
185 determined by a significantly higher Manders' overlap coefficient for *At*SAR1b (**Fig. 2D**).
186 Taken together, these results suggested that when *At*PHT1;1 is overexpressed as a COPII-
187 dependent export membrane cargo, *At*PHF1 can partially distribute into puncta that are
188 associated with ERES markers.
189
190 **The interaction of *At*PHF1 with *At*SAR1b/c *in planta* based on tripartite split-GFP**
191 **association**
192 As *At*PHT1;1 overexpression triggered partial distribution of *At*PHF1 into punctate structures
193 associated with *At*SAR1b and *At*SEC24a, we postulated that *At*PHF1 may participate in COPII
194 recruitment or assembly. To explore this possibility, we examined the interaction of *At*PHF1
195 with several COPII-related components based on the tripartite split-GFP association in agro-
196 infiltrated tobacco leaves (Cabantous et al., 2013; Liu et al., 2018). The expression of split-GFP
197 tagged *At*SEC12 and *At*PHF1 (S10-*At*SEC12 and S10-*At*PHF1) confirmed their localization at
198 the ER when co-expressed with the cytosolic S11-GFP1–9 (**Supplementary Fig. S4B**). We also
199 generated constructs expressing the split-GFP-tagged *At*SAR1c, *At*SEC13a, and *At*SEC16a
200 (*At*SAR1c-, *At*SEC13a-, and *At*SEC16a-S11). As *AtSAR1c* is the second most highly expressed
201 *AtSAR1* gene in roots (Liu et al., 2016) (**Supplementary Fig. S3**) and plays an interchangeable
202 role with *AtSAR1b* at the protein level in pollen development (Liang et al., 2020), we included
203 *At*SAR1c-S11 for comparison with *At*SAR1b. As previously reported (Hanton et al., 2008;
204 Hanton et al., 2009; Takagi et al., 2013), *At*SAR1c-, *At*SEC13a-S11, and *At*SEC16a-S11

205 predominantly localized to the cytosol and ERES puncta (**Supplementary Fig. S4A**). The
206 expression of 3xHA-S11 or S10-3xHA exhibited cytosolic patterns (**Supplementary Fig. S4**)
207 and was used as a negative control for the interaction (**Fig. 3A**–**C**). The interaction of S10-
208 *At*SEC12 with *At*SAR1b- or *At*SAR1c-S11 was used as a positive control, yielding the GFP
209 complementation signals (**Fig. 3A**). Notably, like S10-*At*SEC12, S10-*At*PHF1 interacted with
210 *At*SAR1b- and *At*SAR1c-S11 but not with *At*SEC24a-, *At*SEC13a-, and *At*SEC16a-S11 (**Fig.**
211 **3B**), suggesting the specificity of *At*PHF1 interaction with *At*SAR1s among the COPII-related
212 proteins.
213
214 **The interaction of *At*PHF1 with *At*SAR1b *in planta* based on miniTurbo (mTb) proximity**
215 **labeling**
216 The tripartite split-GFP association detects protein-protein interaction without spurious
217 background signals even when bait and prey proteins are overexpressed (Cabantous et al., 2013;
218 Liu et al., 2018). Still, we employed the proximity labeling method as a complementary
219 approach to validate the *in planta* interaction between *At*PHF1 and *At*SAR1b. Proximity
220 labeling begins after the application of biotin and can be reversibly halted by removing biotin,
221 thereby allowing the capture of transient and dynamic protein-protein interactions at a ten-
222 nanometer scale (Kim et al., 2014; Xu et al., 2023). Due to the superior feasibility of miniTurbo
223 (mTb) in the tobacco system (Mair et al., 2019), the mTb-based proximity labeling was used.
224 For unknown reasons, our initial attempt to express mTb-EYFP-*At*PHF1 in agro-infiltrated
225 tobacco leaves was unsuccessful, so we generated the *At*SAR1b-mTb-S11 construct by fusing
226 mTb to *At*SAR1b (**Fig. 4A**). We used the cytosol-localized mTb-NES-EYFP (**Fig. 4B**), which
227 carries the nuclear export sequence (NES), as a negative control (Mair et al., 2019). Taking
228 advantage that S11 can self-complement with GFP1–10, we could detect the expression and
229 subcellular distribution of *At*SAR1b-mTb-S11 in agro-infiltrated tobacco leaves (**Fig. 4B**). We
230 then co-expressed mTb-NES-EYFP or *At*SAR1b-mTb-S11 with *At*SEC12-mCherry or

231 *At*PHF1-mCherry and incubated the harvested leaves in a biotin solution, followed by tissue
232 homogenization and protein extraction. The protein extraction of non-infiltrated tobacco leaves
233 was used for the background comparison. As the expression of the cytosolic mTb-NES-EYFP
234 was much greater than the membrane-associated *At*SAR1b-mTb-S11, we adjusted the ratio of
235 protein amount for *At*SAR1b-mTb-S11: mTb-NES-EYFP to 30: 1 (**Fig. 4C**; left panel). In this
236 way, the protein amounts of *At*SAR1b-mTb-S11 and mTb-NES-EYFP were comparable,
237 allowing them to fairly compete with binding to streptavidin beads. When co-expressed with
238 *At*SAR1b-mTb-S11, both *At*SEC12-mCherry and *At*PHF1-mCherry could be captured by
239 streptavidin and detected by immunoblot, indicating that they were biotinylated (**Fig. 4C**; left
240 panel). By contrast, the co-expression of mTb-NES-EYFP with *At*SEC12-mCherry or *At*PHF1-
241 mCherry did not yield similar effects (**Fig. 4C**; left panel). Consistently, when equal protein
242 amounts were used for the experiments, even though the expression of *At*SAR1b-mTb-S11 was
243 about five times lower than that of mTb-NES-EYFP, about two times more *At*SEC12-mCherry
244 or *At*PHF1-mCherry was captured by streptavidin when co-expressed with *At*SAR1b-mTb-S11
245 (**Fig. 4C**; right panel). These results again suggested that *At*PHF1 interacts with *At*SAR1s *in*
246 *planta*.
247 To determine which region of *At*PHF1 interacts with *At*SAR1s, we generated four N-terminally
248 S10-tagged *At*PHF1 truncated variants as follows: the cytoplasmic domain alone (*At*PHF1 N),
249 the cytoplasmic domain with the transmembrane (TM) domain (*At*PHF1 N–TM), the TM
250 domain alone (*At*PHF1 TM), and the TM domain with the ER-luminal domain (*At*PHF1 TM–
251 C) (**Supplementary Fig. S6A**). The expression and subcellular distribution of these *At*PHF1
252 variants suggested that the S10-*At*PHF1 N variant was present in the cytosol and nucleus, while
253 the other truncated forms of *At*PHF1 localized to the ER (**Supplementary Fig. S6B**). The
254 subcellular localization of the C-terminally S11-tagged truncated forms of *At*PHF1 also showed
255 similar results (**Supplementary Fig. S6C**), suggesting that the TM domain of *At*PHF1 alone is
256 sufficient for its ER targeting. Of note, the interaction of S10-tagged *At*PHF1 N or *At*PHF1 N–

257 TM with *At*SAR1b- or *At*SAR1c-S11 displayed both the ER and puncta patterns
258 (**Supplementary Fig. S7A** and **S7B**). By contrast, the interaction of S10-tagged *At*PHF1 TM
259 or *At*PHF1 TM–C with *At*SAR1b- or *At*SAR1c-S11 additionally resulted in a few GFP signals
260 that did not display a typical reticular ER pattern (**Supplementary Fig. S7A** and **S7B**). These
261 observations suggest that both the cytosolic and the transmembrane domains of *At*PHF1
262 contribute to the interaction with *At*SAR1s at the ER.
263

264 **Co-immunoprecipitation of the endogenous *At*tPHF1 with *At*SAR1c-GFP in *Arabidopsis***
265 **root**

266 To determine whether the interaction of *At*PHF1 and *At*SAR1s is physiologically relevant, we
267 used *Arabidopsis* transgenic plants expressing *At*SAR1c-GFP or GFP under the UBQ10
268 promoter for co-IP analysis (Zeng et al., 2015). The *Arabidopsis* seedlings were subjected to
269 seven days of Pi starvation to mimic the physiological conditions in which the endogenous
270 *At*PHF1 is upregulated and the ER export of *At*PHT1 proteins is also highly demanded. A total
271 root protein extract was used for GFP-Trap co-IP, followed by immunoblot analysis using an
272 anti-*At*PHF1 antibody. Due to the differences in the expression level between the cytosolic GFP
273 and the membrane-associated *At*SAR1c-GFP in transgenic plants, we increased the protein
274 amount for the co-IP of *At*SAR1c-GFP by 50-fold compared to that for the co-IP of GFP.
275 Immunoblot results suggested that the endogenous *At*PHF1 was co-immunoprecipitated with
276 *At*SAR1c-GFP but not with GFP (**Fig. 5A**). Conversely, when we used equal amounts of root
277 total proteins for co-IP analysis, the expression of *At*SAR1c-GFP was ten times lower than that
278 of GFP but was co-immunoprecipitated about three times more endogenous *At*PHF1 (**Fig. 5B**),
279 suggesting that *At*SAR1c-GFP exhibits a higher binding affinity toward *At*PHF1. Moreover, the
280 endogenous *At*PHT1;1/2/3 proteins could also be co-immunoprecipitated with *At*SAR1c-GFP
281 (**Fig. 5A** and **5B**), indicating the presence of a protein complex containing *At*SAR1s, *At*PHF1,
282 and *At*PHT1s. These data supported the notion that through interacting with *At*SAR1s, *At*PHF1

283 participates in the initial phase of COPII assembly for the ER export of *At*PHT1s.

284

285 ***At*PHF1 preferentially interacts with the GDP-locked inactive form of *At*SAR1b**

286 Because the assembly and disassembly of COPII is controlled by the SAR1 GTPase cycle (Van
287 der Verren and Zanetti, 2023), we next asked whether *At*PHF1 interacts with *At*SAR1s in a
288 specific nucleotide-binding state. Confocal analysis suggested that both the wild-type
289 *At*SAR1b-S11 and the GTP-locked *At*SAR1b[H74L]-S11 localized to the ER membrane and
290 cytosol as previously reported (daSilva et al., 2004; Wei and Wang, 2008) (**Supplementary Fig.**
291 **S4A** and **S8A**). The GDP-locked *At*SAR1b[T34N]-S11 also displayed a similar subcellular
292 pattern (**Supplementary Fig. S8A**). Furthermore, to quantify the soluble and membrane-
293 associated populations of the *At*SAR1b variants, we applied biochemical fractionation.
294 Although the microsomal fraction was slightly contaminated with the soluble fraction, as
295 indicated by the detection of a small amount of cytosolic FBPase, the majority of the *At*SAR1b
296 proteins were membrane-associated (**Supplementary Fig. S8B**). Namely, the membrane-
297 associated proportions of *At*SAR1b-S11, *At*SAR1b[H74L]-S11, and *At*SAR1b[T34N]-S11
298 were 76.4%, 96.1%, and 67.7%, respectively, suggesting that the GDP-locked form of *At*SAR1b
299 is relatively less membrane-associated (**Supplementary Fig. S8B**). These results were in
300 agreement with the previous finding that upon binding of GTP, SAR1 is activated to insert into
301 the ER membrane (d'Enfert, 1991; Paul et al., 2023). More importantly, the *in-planta* tripartite
302 split-GFP assay suggested that, like *At*SEC12, *At*PHF1 preferentially interacts with the GDP-
303 locked form of *At*SAR1b (**Fig. 6A** and **6B**). The interaction of *At*PHF1 N with the *At*SAR1b or
304 the GDP-locked *At*SAR1b[T34N] showed cytoplasmic, ER, and puncta patterns (**Fig. 6B**). By
305 contrast, the interaction of the *At*PHF1 N–TM, *At*PHF1 TM, or *At*PHF1 TM–C variants with
306 *At*SAR1b or the GDP-locked *At*SAR1b[T34N] showed a reticular ER pattern, and occasionally
307 punctate structures at the ER (**Fig. 6B**). Interestingly, the interactions of the *At*PHF1 TM or the
308 *At*PHF1 TM–C with the GTP-locked *At*SAR1b[H74L] were detected at both the ER and the

309 non-ER compartments (**Fig. 6B**). Overall, the GTP-locked *At*SAR1b[H74L] drastically reduced
310 the interaction with the full-length *At*PHF1, *At*PHF1 N and *At*PHF1 N–TM variants (**Fig. 6B**).
311 Compared to the *At*SAR1b, the GTP-locked *At*SAR1b[H74L] slightly increased the interaction
312 with the *At*PHF1 TM and the *At*PHF1 TM–C, which was likely due to a better membrane
313 association of *At*SAR1b[H74L] (**Fig. 6B** and **Supplementary Fig. S8B**). We interpret these as
314 indicating that the removal of the N-terminal cytosolic domain of *At*PHF1 allows a non-specific
315 interaction of *At*PHF1's transmembrane domain with the GTP-locked *At*SAR1b[H74L]. Taken
316 together, these results indicate that the *At*PHF1 variants containing the cytosolic domain
317 preferentially associate with the GDP-bound *At*SAR1 and thus likely participate in recruiting
318 COPII components to ERES. To further support this finding, we performed co-IP assays in
319 transgenic plants expressing *dex:At*SAR1b[H74L]-CFP (Lupanga et al., 2020). Upon
320 dexamethasone (DEX) induction, *At*SAR1b[H74L]-CFP was expressed and detected in the root
321 total protein extracts (**Fig. 6C**). When equal amounts of expressed *At*SAR1c-GFP and GTP-
322 locked *At*SAR1b[H74L]-CFP proteins were used for IP analysis, four times more endogenous
323 *At*PHF1 was co-immunoprecipitated with *At*SAR1c-GFP than with *At*SAR1b[H74L]-CFP (**Fig.**
324 **6C**). These results suggest that GTP-locked *At*SAR1b[H74L]-CFP has a lower binding affinity
325 than *At*SAR1c-GFP toward *At*PHF1 in *Arabidopsis* roots.
326

327 **Discussion**

328 Although several ER accessory proteins have been identified as participating in the ER exit of
329 membrane proteins, the underlying molecular mechanisms are largely unclear (Tang et al., 2005;
330 Bisnett et al., 2020). In *Arabidopsis*, AUXIN RESISTANCE4 (AXR4) was shown to interact
331 with auxin influx carriers AUX1 and LAX2 to promote their PM targeting (Dharmasiri, 2006;
332 Tidy et al., 2024). The KAONASHI3 (KNS3) family was recently identified to mediate the ER
333 exit of the boric acid channel *At*NIP5;1 (Zhang et al., 2024). While *At*PHF1 is required for the
334 PM targeting of *At*PHT1s, it was proposed to act as an ER-localized chaperone for the protein

335 stability of *At*PHT1s (González et al., 2005) and not participate in the COPII vesicle formation
336 (Bayle et al., 2011). On the contrary, our data revealed a role for *At*PHF1 in the early step of
337 COPII assembly through the interaction with *At*SAR1s. Using three different methods—
338 tripartite split-GFP complementation, proximity labeling, and co-immunoprecipitation—we
339 demonstrated that *At*PHF1 interacts with *At*SAR1s *in planta* (**Fig. 3**, **4**, and **5**). Furthermore, the
340 tripartite split-GFP and the co-IP assays demonstrated that *At*PHF1 preferentially interacts with
341 the GDP-bound *At*SAR1s (**Fig. 6**). Our findings uncover that *At*PHF1 likely mediates the
342 assembly of COPII vesicles through interacting with *At*SAR1s, thereby facilitating the ER
343 export of *At*PHT1s (**Fig. 7**). The recruitment of COPII to ERES is increased in response to the
344 demand for ER export of membrane cargoes (Hanton et al., 2007). Our results showed that the
345 transient overexpression of *At*PHT1;1 in *N. benthamiana* leaves also triggered partial
346 distribution of *At*PHF1 into the punctate structures associated with the ERES markers *At*SAR1b
347 and *At*SEC24a (**Fig. 1** and **Fig. 2**). In other words, under an increased demand for the COPII-
348 mediated export of *At*PHT1s, *At*PHF1 may partially relocate to ERES to promote this process.
349
350 The yeast ER membrane-localized chaperone Shr3 is specifically required for proper folding of
351 amino acid permeases and their targeting to the plasma membrane (Kota and Ljungdahl, 2005).
352 Interestingly, the amino acid permease Gap1 split into N- and C-terminal portions can be
353 assembled to form a functional permease in an Shr3-dependent manner (Kota et al., 2007). We
354 also generated the N- and C-terminal portions of *At*PHT1;1 (*At*PHT1;1 TM1–6 half and the
355 *At*PHT1;1 TM7–12 half) to test whether *At*PHF1 plays a critical role in enabling *At*PHT1;1 to
356 fold and attain a proper structure competent for ER export. Even upon overexpression of
357 *At*PHF1, both the *At*PHT1;1 N and C-halves were unable to exit the ER (**Supplementary Fig.**
358 **S9A**). In this scenario, neither the N-half nor the C-half of *At*PHT1;1 resulted in a partial
359 distribution of *At*PHF1 to punctate structures (**Supplementary Fig. S9B** and **S9C**). This
360 indicates that partial recognition of *At*PHT1;1 by *At*PHF1 is insufficient; instead, *At*PHT1;1

361 must attain a functional conformation that enables it to interact properly with *At*PHF1, thereby
362 triggering a signal for ER export.
363 Although *At*PHF1 lacks the conserved residues required for GEF activity and cannot
364 complement the yeast *sec12* growth defect (González et al., 2005), we surmised that upon
365 *At*PHT1;1 overexpression, the distribution of *At*PHF1 to the ERES may facilitate the COPII
366 recruitment or assembly. We reasoned that without co-expression of *At*PHT1s, observing partial
367 co-localization of *At*PHF1 with ERES is beyond the detection limit of confocal imaging, which
368 may explain the discrepancy between our results and those from a previous study (Bayle et al.,
369 2011). In support of this notion, we demonstrated that endogenous *At*PHF1 and *At*PHT1;1/2/3
370 proteins were induced and co-immunoprecipitated with *At*SAR1c-GFP in transgenic plants
371 subjected to Pi starvation (**Fig. 5**), suggesting the physiological relevance of the interaction
372 between *At*PHF1 and *At*SAR1s. In addition, *At*PHF1 interacted with *At*SAR1b and *At*SAR1c
373 but not with other COPII-related components (**Fig. 3B**), and preferentially interacted with the
374 GDP-locked form of *At*SAR1 *in planta* (**Fig. 6**), indicating that *At*PHF1 participates in the early
375 step of COPII assembly, thus likely indirectly assisting the loading of *At*PHT1s into COPII
376 vesicles for the ER export.
377 For unknown reasons, we failed to detect the interaction of *At*PHF1 or *At*SEC12 with *At*SAR1s
378 in the yeast split-ubiquitin system (**Supplementary Fig. S10A** and **S10B**). Similarly, our
379 attempt to compare the interaction strength of the cytosolic N-terminal domain of *At*PHF1 with
380 the GDP- or GTP-bound *At*SAR1b using yeast two-hybrid assays was unsuccessful
381 (**Supplementary Fig. S11**). The failure to detect the interaction between *At*SEC12 or *At*PHF1
382 with *At*SAR1s in yeast may reflect the limitations of the heterologous system. Nevertheless,
383 our findings indicated that *At*PHF1 could link the specific recognition of *At*PHT1s with the
384 modulation of *At*SAR1s activity for the COPII assembly. Such a mechanism differs from that
385 reported for SED4, the yeast structural homolog of SEC12, which also lacks GEF activity
386 (Gimeno, 1995; Kodera et al., 2011). Genetic and biochemical evidence suggested that SED4

387 and SEC12 are not functionally interchangeable and that SED4 weakly inhibits the GTPase-
388 activating (GAP) activity of SEC23 toward SAR1 (Saito-Nakano and Nakano, 2000). On the
389 contrary, an *in vitro* study showed that SED4 had stronger binding to the non-hydrolyzable GTP
390 analog GMPPNP-bound SAR1 and stimulated SEC23 GAP activity, thereby accelerating the
391 dissociation of COPII coats from the ER membrane (Gimeno, 1995; Kodera et al., 2011). While
392 the interaction between SED4 and SEC16 is required for the localization of SEC16 to ERES
393 (Gimeno, 1995), the interaction between *At*PHF1 and *At*SEC16a was not observed (**Fig. 3B**).
394 As many COPII-related factors regulate SAR1 activity through direct or indirect interaction
395 (Van der Verren and Zanetti, 2023), we propose that PHF1 modulates the recruitment efficiency
396 of SAR1s to ERES, thereby facilitating the formation of COPII vesicles to carry PHT1s (**Fig.**
397 **7**). Nevertheless, we do not exclude the possibility that PHF1 plays dual roles, acting as a
398 membrane chaperone for the correct folding of newly synthesized PHT1s in the ER and also
399 mediating COPII assembly. Without uncoupling these two potential functions of PHF1, its role
400 as a chaperone at an earlier step will mask the involvement of PHF1 in the re-localization of
401 PHT1s to ERES at a later step.
402 Interestingly, we recently reported that the *Arabidopsis* CORNICHON HOMOLOG 5
403 (*At*CNIH5) acts as an ER cargo receptor that cycles between the ER and the early Golgi and
404 selects *At*PHT1s for ER export (Chiu, 2024; Liu et al., 2025). As the *cnih5 phf1* mutant shows
405 more severe growth defects than the *phf1* single mutant, and *At*PHF1 proteins are increased in
406 the root of *cnih5* (Chiu, 2024), we suspected that *At*PHF1 and *At*CNIH5 work interdependently.
407 Namely, while *At*PHF1 couples the recognition of *At*PHT1s and the recruitment of COPII
408 proteins by interacting with *At*PHT1s and *At*SAR1s, *At*CNIH5 is involved in the selective
409 packaging of *At*PHT1 into COPII vesicles.
410 *At*PHF1 is structurally related to SEC12 proteins, which adopt a seven-bladed β propeller
411 (González et al., 2005; Joiner and Fromme, 2021). Based on the crystal structure, the
412 catalytically critical K loop within the cytoplasmic domain of yeast SEC12 makes direct contact

413 with nucleotide-free SAR1 (McMahon et al., 2012; Joiner and Fromme, 2021). By contrast, our
414 data showed that both the cytosolic and the transmembrane domains of *At*PHF1 interact with
415 *At*SAR1b/c *in planta* (**Supplementary Fig. S7A** and **S7B**), indicating that the interaction
416 interface may span relatively large areas. Since the catalytic residues required for GEF activity
417 are not conserved in *At*PHF1 (González et al., 2005), it remains to be elucidated whether the
418 interaction interface of PHF1-SAR1s is different from that of SEC12-SAR1s and how PHF1
419 modulates the recruitment of SAR1s without GEF activity.
420

421 **Materials and Methods**

422 **Plant material and growth conditions**

423 The seeds of *Arabidopsis thaliana* wild-type (WT) (Columbia, Col-0) and *phf1* were obtained
424 from the Arabidopsis Biological Resource Center (ABRC). Seeds of *A. thaliana* were surface-
425 sterilized and germinated on half-strength modified Hoagland agar plates (Millner, 1992; Liu
426 et al., 2012) and grown in the growth chamber at 22°C under a 16-h-light/8-h-dark cycle. The
427 Pi-sufficient (+P) and Pi-deficient (−P) media were half-strength modified Hoagland nutrient
428 solutions containing 250 μM and 0 μM KH_2PO_4, respectively. Seeds of *Nicotiana benthamiana*
429 (*N. benthamiana*) were surface-sterilized and germinated on half-strength Murashige and
430 Skoog medium and grown in the growth chamber at 24°C under a 16-h-light/8-h-dark cycle.
431

432 **Plasmid construction**

433 For the self-complementing split-GFP assay (Liu et al., 2018), the constructs encoding
434 *UBQ10:sXVE:*GFP1–10 (Addgene plasmid #125663), *UBQ10:sXVE:*ER-GFP1–10 (Addgene
435 plasmid #125664) or *UBQ10:sXVE:*S11-GFP1–9 (Addgene plasmid #125665) was used. For
436 the tripartite split-GFP association, the constructs encoding *UBQ10:sXVE:*GFP1–9 (Addgene
437 plasmid #108187) or *35S:*GFP1–9.pMDC201 were used. The CDS of GFP1–9 was amplified
438 by PCR using *P16ΔS:*GFP1–9 (Addgene plasmid #108186) as the template and subcloned into

439 pMDC201, yielding *35S:*GFP1–9.pMDC201. For constructing the S10-tagged clones, the CDS
440 of full-length and truncated *At*PHF1 and *At*PHT1;1 were amplified by PCR and subcloned into
441 *UBQ10:XVE:*S10-(MCS) (Addgene plasmid #108177), in which the inducible promoter
442 *UBQ10:sXVE* was replaced by the *UBQ10* promoter to generate *UBQ10:*S10-(MCS). The CDS
443 of *At*SEC12 and *At*PHF1 were amplified by PCR and subcloned into *UBQ10:*S10-(MCS). For
444 constructing the S11-tagged clones, the CDS of *At*PHT1;1 was amplified by PCR and subcloned
445 into *UBQ10:sXVE:*(MCS)-3xHA-S11 (Addgene plasmid #108180). The CDS of *At*STP1 and
446 *At*PHT1;1 and truncated *At*PHF1 were amplified by PCR and subcloned into
447 *UBQ10:sXVE:*(MCS)-S11 (Addgene plasmid #108179), in which the inducible promoter
448 *UBQ10:sXVE* was replaced by the *UBQ10* promoter to generate *UBQ10:*(MCS)-S11. The CDS
449 of *At*SAR1b, *At*SAR1b[H74L] (Takeuchi, 2000), *At*SAR1b[T34N], *At*SAR1c, *At*SEC24a,
450 *At*SEC13a, and *At*SEC16a were amplified and subcloned into *UBQ10:*(MCS)-S11. For
451 constructing the GFP fusion clones, the inducible promoter *UBQ10:sXVE* of
452 *UBQ10:sXVE:*(MCS)-GFP (Schlücking et al., 2013) was replaced by the *UBQ10* promoter to
453 generate *UBQ10:*(MCS)-GFP. The CDS of *At*PHF1 was amplified and subcloned into
454 *UBQ10:*(MCS)-GFP. For constructing the mCherry fusion clones, the GFP of
455 *UBQ10:sXVE:*(MCS)-GFP (Schlücking et al., 2013) was replaced by mCherry to generate
456 *UBQ10:sXVE:*(MCS)-mCherry. The CDS of *At*SEC12 was amplified and subcloned into
457 *UBQ10:sXVE:*(MCS)-mCherry, followed by replacing the inducible promoter with the *UBQ10*
458 promoter to generate *UBQ10:At*SEC12-mCherry. The CDS of mTb was amplified by PCR
459 using R4pGWB601_UBQ10p-miniTurbo-NES-YFP (Addgene plasmid #127369) as the
460 template and subcloned into *UBQ10:At*SAR1b-S11, yielding *UBQ10:At*SAR1b-mTb-S11. The
461 abovementioned constructs were generated either by restriction enzyme cloning or by In-
462 Fusion® HD cloning (Takara). Primer sequences and the restriction enzyme cutting sites used
463 are listed in **Supplementary Table S1**.
464

465 **Agro-infiltration of *Nicotiana benthamiana* leaves**

466 Three-to-four-week-old *Nicotiana benthamiana* plants were used for *A. tumefaciens* (strain
467 EHA105)-mediated infiltration. The bacterial cultures were grown overnight in Luria-Bertani
468 (LB) medium containing the appropriate antibiotics (50 μg/ml spectinomycin, 5 μg/ml
469 rifampicin, or 50 μg/ml kanamycin) at 30°C with shaking at 200 rpm. Cells were pelleted and
470 resuspended in infiltration buffer containing 10 mM $MgCl_2$, 10 mM MES (pH 7.5), and 150
471 μM acetosyringone to an OD_{600} of 1.0 and incubated at room temperature (RT) for 2–4 h. Leaf
472 infiltration was performed with agrobacterial suspensions at a final OD_{600} of 0.002–1.0. For
473 *UBQ10:sXVE*-inducible expression, 9.18 μM β-estradiol was applied for an additional 24 or 48
474 h. Leaves were harvested at 48 or 72 h post-infiltration for confocal microscopy or protein
475 extraction.

476

477 **Confocal image analysis**

478 Confocal images were captured using the Zeiss LSM 800 microscope (Zeiss) equipped with
479 Plan-Apochromat 10×/0.45 M27, 20×/0.8 M27, and 40×/1.3 Oil DIC M27 objectives. The
480 acquisition was performed in multi-track mode with line switching, and the data were averaged
481 over two readings. Excitation/emission wavelengths were 488 nm/410–546 nm and 561
482 nm/560–617 nm for GFP and mCherry, respectively.

483

484 **Soluble and microsomal protein extraction**

485 Soluble (S) and microsomal (M) fractions were prepared from agro-infiltrated *N. benthamiana*
486 leaves with the modified low-speed pellet (LSP) method (Yoshimoto et al., 2004). Leaf tissues
487 were ground in liquid nitrogen (N) and resuspended in three volumes (3 ml per gram tissue) of
488 pre-chilled LSP buffer containing 100 mM Tris-HCl (pH 7.5), 400 mM sucrose, 1 mM EDTA,
489 1% Triton X-100, 0.1 mM phenylmethylsulfonyl fluoride (PMSF), and 1× Protease Inhibitor
490 Cocktail (P9599, Sigma-Aldrich). After centrifugation at 500 × g for 5 min and then at 13,000

491 × g for 15 min at 4°C, the final supernatant was collected as the soluble fraction. The pellet was
492 resuspended in pre-chilled LSP buffer lacking 1% Triton X-100 to yield the microsomal fraction.
493
494 **Proximity labeling assay**
495 The *N. benthamiana* leaves were incubated in 50 μM biotin solution at RT for 30 min, ground
496 with liquid N, and extracted in two volumes (2 ml per gram tissue) of lysis buffer containing
497 20 mM HEPES (pH 7.5), 40 mM KCl, 1 mM EDTA, 1% Triton X-100, 0.2 mM PMSF, and 1×
498 Protease Inhibitor Cocktail (P9599, Sigma-Aldrich). After centrifugation at 4,000 × g for 5 min
499 and then at 20,000 × g for 15 min at 4°C, the resulting supernatant was collected. A 25–750 μg
500 of the crude extract was incubated with 5 μl Streptavidin-agarose (S1638, Sigma-Aldrich) at
501 4°C overnight under 5 rpm end-to-end rotation. The beads collected by centrifugation at 2,500
502 × g and 4 °C for 5 min were washed with a lysis buffer containing 0.1% Triton X-100 once.
503 After centrifugation at 2,500 × g for 5 min at 4°C, the beads were eluted with 2× SDS sample
504 buffer containing 100 mM Tris-HCl (pH 6.8), 20% glycerol, 4% SDS, and 100 mM
505 dithiothreitol (DTT) with 0.4 M urea.
506
507 **Co-immunoprecipitation assay**
508 The 11-day-old Col-0, *UBQ10:*GFP, *UBQ10:At*SAR1c-GFP (Zeng et al., 2015), and
509 *dex:At*SAR1b[H74L]-CFP (Lupanga et al., 2020) seedlings were grown with 7 days of Pi
510 starvation. The seedlings of *dex:At*SAR1b[H74L]-CFP were treated with 10 μM
511 dexamethasone (DEX) or DMSO for an additional 24 h before root collection. The roots were
512 harvested for total protein extraction with lysis buffer containing 25 mM HEPES (pH 7.2), 150
513 mM NaCl, 0.5% IGEPAL CA-630 (I8896, Sigma-Aldrich), 2 mM EDTA, 0.5 mM $MgCl_2$, and
514 1× Protease Inhibitor Cocktail (P9599, Sigma-Aldrich). After centrifugation at 16,000 × g for
515 5 min at 4°C, supernatants were cross-linked with 2.5 mM dithiobis [succinimidyl propionate]
516 (DSP) at RT for 30 min and quenched with 100 mM Tris (pH 7.4) for 15 min. A 15–750 μg of

517 protein mixture was incubated with 5 µl of GFP-Trap® Agarose (ChromoTek) at 4°C for 2 h
518 with end-over-end rotation at 5 rpm, washed with the lysis buffer once, centrifuged at 2,500 ×
519 g at 4°C for 5 min, and eluted with 2× SDS sample buffer containing 100 mM Tris-HCl (pH
520 6.8), 20% glycerol, 4% SDS, and 100 mM DTT.
521
522 **Immunoblot analysis**
523 Protein samples were loaded onto 4–12% Q-PAGE™ Bis-Tris Precast Gel (SMOBIO) and
524 transferred to polyvinylidene difluoride (PVDF) membranes (IPVH00010 Immobilon-P
525 Membrane, Merck). The membrane was blocked with 1% BSA in 1× PBS solution containing
526 0.2% Tween 20 (PBST, pH 7.2) at RT for 1 h and hybridized with primary antibodies: anti-GFP
527 (1:5,000, AS21 4696; Agrisera) at 4°C for overnight, anti-*At*PHT1;1/2/3 (1:1,000, PHY0753;
528 PhytoAB) at 4°C for overnight, anti-*At*PHF1 (Huang et al., 2013) at RT for 2 h, anti-PIP2;7
529 (1:5,000, AS22 4812, Agrisera) at RT for 1 h, anti-cFBPase (1:5000, AS04 043, Agrisera) at
530 4°C for overnight, anti-mCherry (1:1,000, ab167453, Abcam) at RT for 1 h, and anti-S11
531 (1:10,000) at RT for 1 h, the anti-S11 polyclonal rabbit antibody was raised against the peptide
532 of S11 (EKRDHMVLLEYVTAAGITDASC) and produced by LTK BioLaboratories, Taiwan.
533 The membrane was washed four times with 1× PBST for 5 min, followed by hybridization with
534 the horseradish peroxidase-conjugated secondary antibody (1:20,000–1:40,000, GTX213110-
535 01 and 1:10,000, GTX213111-01, GeneTex) in blocking solution at RT for 1 h. After four
536 washes in 1× PBST for 5 min and a rinse with distilled water, chemiluminescent substrates
537 (WesternBright™ ECL and WesternBright™ Sirius, Advansta) for signal detection were
538 applied.
539
540 **Quantification analyses**
541 For puncta quantification, two non-overlapping regions of interest (ROIs, 1000 µm²) were
542 randomly selected from a single confocal image (53.24 × 53.24 µm²). For each ROI, the

543 automatic Triangle threshold was applied. Punctate structures were defined using the ImageJ
544 (Schneider et al., 2012) 'analyze particles' function with circularity from 0.1 to 1.0 and size
545 from 0.04 to infinity. Colocalization analysis was performed with a Costes' automatic threshold,
546 and Manders' overlap coefficients were calculated using the JACoP plugin with object-based
547 method in Fiji (Bolte and Cordelieres, 2006). The Dunnett's test and Mann-Whitney U test were
548 performed using JASP 0.95.4.0. Puncta diameters were measured by using the Zeiss ZEN 3.7
549 software. The box plots were generated by using BoxPlotR (Spitzer et al., 2014).
550
551 **Chemical treatment**
552 Acetosyringone (150 mM stock in DMSO, D134406, Sigma-Aldrich) was diluted to a final
553 concentration of 150 μM in ddH_2O. β-estradiol (36.7 mM stock in ethanol, E2758, Sigma-
554 Aldrich) was diluted to a final concentration of 9.18 μM in ddH_2O. Dithiobis [succinimidyl
555 propionate] (25 mM stock in DMSO, 22586, ThermoFisher) was diluted to a final concentration
556 of 2.5 mM in ddH_2O. Dexamethasone (100 mM stock in DMSO, D4902, Sigma-Aldrich) was
557 diluted to a final concentration of 10 μM in ddH_2O.
558
559 **Accession Numbers**
560 Sequence data from this article can be found in the Arabidopsis Genome Initiative under the
561 following accession numbers: *At*PHF1 (AT3G52190), *At*SEC12 (AT2G01470), *At*PHT1;1
562 (AT5G43350), *At*STP1 (AT1G11260), *At*SAR1b (AT1G56330), *At*SAR1c (AT4G02080),
563 *At*SEC24a (AT3G07100), *At*SEC13a (AT3G01340), *At*SEC16a (AT5G47480).
564
565 **Supplementary Data**
566 **Supplementary Fig. S1. Expression of ER lumen marker in the absence and presence of**
567 ***At*PHT1;1 overexpression.** Representative confocal images **(A)** and quantification of
568 mCherry-HDEL-labeled puncta **(B)** are shown from three independent experiments. Scale bars,

569 20 μm. Box plots show medians (center lines), interquartile ranges (boxes), and data ranges
570 (whiskers), along with individual data points (dots). The number of regions of interest (ROI)
571 used for quantification is shown in parentheses. Not significant, n.s. (Student's t-test against
572 mCherry-HDEL expressed alone).
573
574 **Supplementary Fig. S2. Size analysis of *At*PHF1-GFP- and mCherry-HDEL-labeled**
575 **puncta in the presence of *At*PHT1;1-S11 overexpression. (A)** Quantification of puncta
576 number upon overexpression with *At*PHT1;1-S11, corresponding to Fig. 1D. Data were
577 collected from three independent experiments (Exp. 1, Exp. 2, and Exp. 3). **(B)** Size distribution
578 of overlapping and non-overlapping puncta labeled by *At*PHF1-GFP or the ER luminal marker
579 mCherry-HDEL, corresponding to (**A**). Box plots show medians (center lines), interquartile
580 ranges (boxes), and data ranges (whiskers), along with individual data points (dots). The
581 number of puncta used for quantification is shown in parentheses. Dunnett's test for multiple
582 comparisons against overlapping puncta. Not significant, n.s..
583
584 **Supplementary Fig. S3. Expression of *AtSAR1* isoforms in Col-0 under Pi deprivation by**
585 **RNA-seq analysis.** Expression of *AtSAR1a/b/c/d/e* in the shoot and root of 10-day-old WT
586 (Col-0) seedlings under Pi-sufficient conditions (+P0) or under one day (–P1) and three days of
587 Pi starvation (–P3) as previously described (Liu et al., 2016). RPKM stands for reads per
588 kilobase of transcript per million mapped reads. Numbers represent average RPKM values of
589 two replicates, with an assigned value of 0.25 for readings below this threshold.
590
591 **Supplementary Fig. S4. The expression and distribution of COPII-related components in**
592 **agro-infiltrated *N. benthamiana* leaves. (A)** Expression and distribution of S11-tagged
593 *At*SAR1b, *At*SAR1c, *At*SEC24a, *At*SEC13a, and *At*SEC16a at the peripheral layer and 3xHA-
594 S11 at the middle layer of agro-infiltrated tobacco epidermal cells. **(B)** Expression and

595 distribution of S10-tagged *At*SEC12, *At*PHF1, and 3xHA at the middle layer of agro-infiltrated
596 tobacco epidermal cells. Scale bars, 5 μm. Representative confocal images are shown from
597 three independent experiments.
598
599 **Supplementary Fig. S5. Quantification of puncta sizes upon co-expression of *At*PHF1-**
600 **mCherry and *At*PHT1;1 with ERES markers. (A, B)** Quantification of puncta number upon
601 overexpression with *At*SAR1b-S11 (**A**) or *At*SEC24a-S11 (**B**), corresponding to Fig. 2C. Data
602 were collected from three independent experiments (Exp. 1, Exp. 2, and Exp. 3). **(C, D)** Size
603 distribution of overlapping and non-overlapping puncta labeled by *At*PHF1-mCherry or ERES
604 markers, corresponding to (**A**) and (**B**), respectively. Box plots show medians (center lines),
605 interquartile ranges (boxes), and data ranges (whiskers), along with individual data points (dots).
606 The number of puncta used for quantification is shown in parentheses. Dunnett's test for
607 multiple comparisons against overlapping puncta. Not significant, n.s..
608
609 **Supplementary Fig. S6. Expression and subcellular distribution of the truncated *At*PHF1**
610 **variants in agro-infiltrated *N. benthamiana* leaves. (A)** Schematic diagrams of the truncated
611 *At*PHF1 variants with domain boundaries indicated by amino acid numbers. **(B, C)** The
612 expression and distribution of the S10-tagged (**B**) and the S11-tagged (**C**) truncated *At*PHF1
613 variants at the middle layer of epidermal cells. Scale bars, 20 μm. Representative confocal
614 images are shown from three independent experiments.
615
616 **Supplementary Fig. S7. *At*SAR1b and *At*SAR1c interact with the cytosolic and**
617 **transmembrane domains of *At*PHF1 in agro-infiltrated *N. benthamiana* leaves. (A–C)**
618 The interaction analyses of the S10-*At*PHF1 truncated variants with *At*SAR1b-S11 (**A**),
619 *At*SAR1c-S11 (**B**), and 3xHA-S11 (**C**) by using the tripartite split-GFP assay. The interactions
620 with 3xHA-S11 were used as negative controls. Scale bars, 10 μm. Representative confocal

621 images taken at the peripheral layer of the epidermis are shown from at least three independent
622 experiments.
623
624 **Supplementary Fig. S8. Distribution of *At*SAR1b/[H74L]/[T34N] in the agro-infiltrated *N.***
625 ***benthamiana* leaves. (A)** The expression and distribution of the S11-tagged GTP-locked
626 ([H74L]) and GDP-locked *At*SAR1b ([T34N]) at the peripheral layer of epidermal cells. Scale
627 bars, 5 µm. Representative confocal images are shown from three independent experiments. **(B)**
628 Protein expression of *At*SAR1b/[H74L]/[T34N] in the soluble (S) and microsomal (M) fractions
629 isolated using the modified low-speed pellet (LSP) method (Yoshimoto et al., 2004). Anti-S11
630 antibody was used to detect S11 fusion proteins. The membrane association percentage (%) was
631 calculated as M/(S+M) and is shown as mean ± SE from two independent experiments.
632 Aquaporin PIP2;7 and cytosolic fructose-1,6-bisphosphatase (cFBPase) served as microsomal
633 and soluble controls, respectively. Amido black staining was used as a loading control.
634
635 **Supplementary Fig. S9. ER export-incompetent *At*PHT1;1 overexpression cannot trigger**
636 **partial distribution of *At*PHF1 to punctate structures in agro-infiltrated *N. benthamiana***
637 **leaves. (A)** Expression and distribution of S10-*At*PHT1;1 TM1–6 and *At*PHT1;1 TM7–12-S11
638 upon co-expression with *At*PHF1-mCherry in agro-infiltrated tobacco epidermal cells. Scale
639 bars, 5 µm. Representative confocal images taken at the peripheral layer of epidermal cells are
640 shown from three independent experiments. **(B)** Distribution of *At*PHF1-GFP in the presence
641 of S10-*At*PHT1;1 TM1–6 or *At*PHT1;1 TM7–12-S11 co-expression. Scale bars, 5 µm.
642 Representative confocal images are shown from three independent experiments. **(C)**
643 Quantification of *At*PHF1-GFP-labeled punctate structures in (**B**). The data for *At*PHF1-GFP
644 expressed alone are the same as those shown in Fig. 1B. Box plots display medians (center
645 lines), interquartile ranges (boxes), and data ranges (whiskers), along with individual data
646 points (dots). The number of regions of interest used for quantification is shown in parentheses.

647 Dunnett's test for multiple comparisons against *At*PHF1-GFP expressed alone. Not significant,
648 n.s..
649
650 **Supplementary Fig. S10. Interaction analysis of *At*PHF1 with *At*SAR1 in the yeast split-**
651 **ubiquitin system. (A)** Co-expression of *At*PHF1-CubPLV with NubG-*At*PHT1;1, *At*SAR1b-
652 NubG or *At*SAR1c-NubG. **(B)** Co-expression of *At*SEC12-CubPLV with *At*SAR1b-NubG and
653 *At*SAR1c-NubG. The co-expression of *At*PHF1-CubPLV or *At*SEC12-CubPLV with NubWT
654 was used as a positive control, while the co-expression with NubG was used as a negative
655 control. The CDS of *At*PHF1, *At*SEC12, *At*PHT1;1, *At*SAR1b, and *At*SAR1c were amplified by
656 PCR, cloned into the pCR8/GW/TOPO, verified by sequencing, and recombined into
657 destination vectors via LR reactions. *At*PHF1 and *At*SEC12 were cloned into synthesized
658 MET17-PLVCub_GW (Chiu, 2024) to generate C-terminal Protein A–LexA–VP16–Cub
659 fusions (*At*PHF1-CubPLV and *At*SEC12-CubPLV); *At*PHT1;1 was cloned into NX32_GW
660 (ABRC plasmid CD3-1737) to produce NubG-*At*PHT1;1; *At*SAR1b and *At*SAR1c were cloned
661 into XN22_GW (ABRC plasmid CD3-1735) to produce *At*SAR1b-NubG and *At*SAR1c-NubG.
662 Yeast transformants were grown on synthetic medium lacking tryptophan and leucine (SC–WL)
663 for growth detection or on synthetic medium lacking tryptophan, leucine, adenine, and histidine
664 containing 0.5 μM methionine (SC–WLAH + M) for testing protein-protein interaction.
665 Representative results are shown from two independent experiments.
666
667 **Supplementary Fig. S11. Interaction analysis of the N-terminal cytosolic domain of**
668 ***At*PHF1 with *At*SAR1b/[H74L]/[T34N] in the yeast two-hybrid assay.** GAL4[BD]-S10-
669 *At*PHF1 N was co-expressed with GAL4[AD]-*At*SAR1b-S11, GAL4[AD]-*At*SAR1b[H74L]-
670 S11, or GAL4[AD]-*At*SAR1b[T34N]-S11. The co-expression of Krev1 with RalGDS-wt,
671 RalGDS-m1, and RalGDS-m2 were strong positive, weak positive, and negative controls,
672 respectively. The CDS of *At*SAR1b-S11, *At*SAR1b[H74L]-S11, and *At*SAR1b[T34N]-S11 were

673 subcloned into pCR8/GW/TOPO and recombined into pDEST22 via LR reaction to generate
674 GAL4[AD]-*At*SAR1b/[H74L]/[T34N]-S11; the CDS of S10-*At*PHF1 N was subcloned into
675 pCR8/GW/TOPO and recombined into pDEST32 via LR reaction to generate GAL4[BD]-S10-
676 *At*PHF1 N. Yeast transformants were grown on synthetic medium lacking tryptophan and
677 leucine (SC–WL) for growth detection, and on medium lacking tryptophan, leucine, and uracil
678 (SC–WLU) or lacking tryptophan, leucine, and histidine with 10 mM 3-Amino-1,2,4-triazole
679 (SC–WLH + 3AT) to assess protein-protein interactions. Representative results are shown from
680 two independent experiments.
681
682 **Supplementary Table S1. Oligonucleotides used for plasmid constructs.**
683
684 **Funding**
685 This work was supported by the Ministry of Science and Technology (MOST 108-2311-B-007-
686 003-MY3) and the National Science and Technology Council (NSTC 112-2313-B-007-001-
687 MY3).
688
689 **Acknowledgments**
690 We thank Dr. Liwen Jiang at the Chinese University of Hong Kong, People's Republic of China,
691 for sharing the *Arabidopsis* seeds of *UBQ10:At*SAR1c-GFP and *UBQ10:*GFP homozygous
692 lines, Dr. Masaki Takeuchi at the University of Tokyo, Japan, for sharing the clone
693 *35S:At*SAR1b[H74L], Dr. Tzyy-Jen Chiou at Academia Sinica, Taiwan (R.O.C.), for sharing
694 the clone *35S:At*PHF1-mCherry, and Dr. Karin Schumacher at the Cell Biology Research Group
695 of the Centre for Organismal Studies (COS), Heidelberg University, Germany, for sharing the
696 *Arabidopsis* seeds of *dex:At*SAR1b[H74L]-CFP T2 lines. We acknowledge Ms. Wen-Chun
697 Chou for constructing the plasmid encoding *35S:*GFP1–10 and the technical support from the

Confocal Image Core, National Tsing Hua University (sponsored by MOST 108-2731-M-007-001 and MOST 110-2731-M-007-001).

Author Contributions

T.-Y. L. conceived the original research plan, designed and supervised the experiments, and wrote the article. H.-F. L. designed and performed the experiments, analyzed the data, wrote the article, and contributed to the preparation of figures. J.-D. C. designed and performed the experiments.

Conflicts of Interest

The authors declare no conflicts of interest.

Data Availability Statement

All study data are included in the article and/or Supporting Material.

Figure Legends

Figure 1. *At*PHT1;1 overexpression triggers partial distribution of *At*PHF1 to punctate structures in agro-infiltrated *N. benthamiana* leaves. **(A)** Distribution of *At*PHF1-GFP in the absence or presence of *At*PHT1;1-S11 or *At*STP1-S11 co-expression. Arrows, punctate structures. **(B)** Quantification analysis of (**A**) from three independent experiments. **(C)** Co-localization analysis of *At*PHF1-GFP puncta and mCherry-HDEL puncta in the presence of *At*PHT1;1-S11 or *At*STP1-S11 co-expression. Arrows, overlapping puncta; circles, non-overlapping puncta. **(D)** The quantification of (**C**) from three independent experiments. Representative confocal images at the peripheral layers of the epidermis are shown in (**A**) and (**C**); scale bars, 5 μm. Box plots show medians (center lines), interquartile ranges (boxes), data ranges (whiskers), and data points (dots) in (**B**) and (**D**). The number of regions of interest used

724 for quantification is shown in parentheses. ***, $P < 0.001$ versus *At*PHF1-GFP expression alone
725 in (**B**); *, $P < 0.05$ versus overlapping puncta in (**D**); Dunnett's test for multiple comparisons.
726
727 **Figure 2. *At*PHT1;1-induced *At*PHF1 puncta partially co-localize with the ERES markers**
728 **in agro-infiltrated *N. benthamiana* leaves. (A, B)** Co-localization of *At*SAR1b-S11 (**A**) and
729 *At*SEC24a-S11 (**B**) with *At*PHF1-mCherry in the absence or presence of *At*PHT1;1
730 overexpression. Representative confocal images were taken at the peripheral layer of the
731 epidermis. Arrows, overlapping puncta; circles, non-overlapping puncta. Scale bars, 5 µm. **(C)**
732 Quantification of co-localization in (**A**) and (**B**). The number of regions of interest used for
733 quantification is shown in parentheses. *, $P < 0.05$; ***, $P < 0.001$; Dunnett's test for multiple
734 comparisons against overlapping with *At*SAR1b or *At*SEC24a. **(D)** Comparison of Manders'
735 overlap coefficient between the co-localization of *At*PHF1-mCherry with *At*SAR1b-S11 and
736 *At*SEC24a-S11. Data were collected from three independent experiments. Box plots show
737 medians (center lines), interquartile ranges (boxes), data ranges (whiskers), and data points
738 (dots). The puncta numbers used for the quantification analysis are shown in parentheses. *, P
739 < 0.05; two-tailed Mann-Whitney U test.
740
741 **Figure 3. *At*PHF1 interacts with *At*SAR1b and *At*SAR1c *in planta* based on the tripartite**
742 **split-GFP association in agro-infiltrated *N. benthamiana* leaves.** The interaction of S10-
743 *At*SEC12 **(A)** or S10-*At*PHF1 **(B)** with the COPII-related components, *At*SAR1b-, *At*SAR1c-,
744 *At*SEC24a-, *At*SEC13a-, and *At*SEC16a-S11. The interactions with 3xHA-S11 in (**A**) and (**B**)
745 and S10-3xHA (**C**) were used as negative controls. Scale bars, 5 µm. Representative confocal
746 images taken at the peripheral layer of the epidermis are shown from three independent
747 experiments.
748

749 **Figure 4. *At*PHF1 interacts with *At*SAR1b *in planta* based on the proximity labeling in**
750 **agro-infiltrated *N. benthamiana* leaves. (A)** Schematic diagrams of mTb-fused bait protein in
751 the proximity of the prey protein. The reactive intermediate biotinyl-5'-AMP biotinylates
752 proximal prey proteins within the indicated range (grey zone). **(B)** The expression and
753 subcellular distribution of mTb-NES-EYFP and *At*SAR1b-mTb-S11. Scale bars, 20 μm.
754 Representative confocal images are shown from three independent experiments. **(C)** The
755 interaction analyses of *At*PHF1-mCherry and *At*SAR1b by proximity labeling. In the left panel,
756 thirty-fold more protein extract expressing *At*SAR1b-mTb-S11 was used as input for
757 Streptavidin pulldown relative to that expressing mTb-NES-EYFP; in the right panel, equal
758 amounts of protein from the samples were used for pulldown. Anti-S11 antibody was used to
759 detect EYFP-tagged and S11-tagged fusion proteins. Representative results are shown from two
760 independent experiments.
761
762 **Figure 5. Co-immunoprecipitation of the endogenous *At*PHF1 and *At*PHT1;1/2/3 with**
763 ***At*SAR1c-GFP in *Arabidopsis* transgenic plants. (A, B)** The interaction analyses of *At*SAR1c-
764 GFP with the endogenous *At*PHF1 and *At*PHT1;1/2/3 in 11-day-old wild-type (Col-0),
765 *UBQ10:*GFP, and *UBQ10:At*SAR1c-GFP seedlings subjected to Pi deprivation (0 μM KH_2PO_4,
766 7 days of starvation). Fifty-fold more protein extract expressing *At*SAR1c-GFP was used as
767 input for GFP-Trap co-immunoprecipitation relative to that expressing free GFP in (**A**). Equal
768 amounts of protein from the samples were used for co-immunoprecipitation in (**B**). Anti-S11
769 antibody was used to detect GFP fusion proteins. Representative results are shown from three
770 independent experiments.
771
772 **Figure 6. *At*PHF1 preferentially interacts with the GDP-locked form of *At*SAR1b in agro-**
773 **infiltrated *N. benthamiana* leaves and *Arabidopsis* transgenic plants. (A, B)** The interaction
774 analyses of S10-*At*SEC12 (**A**) and S10-*At*PHF1 variants (**B**) with *At*SAR1b/[H74L]/[T34N]-

775 S11 in agro-infiltrated tobacco leaves. Representative confocal images were taken at the
776 peripheral layer of the epidermis. Scale bars, 2 μm. Quantification indicates the number of cells
777 expressing GFP signals per unit leaf area (mm^2). Data were collected from three independent
778 experiments; the number of confocal images (0.32 x 0.32 mm^2) used for quantification is shown
779 in parentheses. **, $P < 0.01$; ***, $P < 0.001$; Dunnett's test for multiple comparisons against
780 *At*SAR1b[H74L]. Not significant, n.s.. **(C)** Interaction analyses of the WT or GTP-locked form
781 of *At*SAR1 with the endogenous *At*PHF1 were performed in 11-day-old *UBQ10:At*SAR1c-GFP
782 and *dex:At*SAR1b[H74L]-CFP seedlings subjected to Pi deprivation (0 μM KH_2PO_4, 7 days).
783 *dex:At*SAR1b[H74L]-CFP seedlings were treated with 24 hours of 10 μM dexamethasone
784 (DEX) or DMSO. The protein amounts as input for GFP-Trap co-immunoprecipitation are as
785 indicated above the image. An anti-GFP antibody was used to detect GFP and CFP fusion
786 proteins. The relative intensity is shown as mean ± SE from two independent experiments.
787
788 **Figure 7. Hypothetical model depicting a role for *At*PHF1 in COPII recruitment for the**
789 **ER export of *At*PHT1 transporters.** The GEF SEC12 recruits and activates SAR1 GTPase by
790 exchanging GDP for GTP. The direct interaction of GTP-bound SAR1 with SEC23 recruits
791 SEC23/24 to form the inner coat, followed by SEC13/31 recruitment to form the outer coat.
792 The ER-resident PHF1 concentrates on ERES triggered by increased PHT1 proteins and
793 interacts with GDP-bound SAR1. While the scaffold protein SEC16 at ERES does not interact
794 with PHF1, the interaction of PHF1 and SAR1 may link to the regulation of SAR1 GTPase
795 recruitment, thereby facilitating COPII assembly at ERES for the ER-to-Golgi transport of
796 PHT1 proteins in the budding COPII vesicles.
797
798 **References**
799 **Bannykh SI, Rowe, T., & Balch, W. E.** (1996) The organization of endoplasmic reticulum export
800 complexes. The Journal of cell biology **135:** 19-35

801 **Barlowe CK, Miller EA** (2013) Secretory protein biogenesis and traffic in the early secretory
802 pathway. Genetics **193:** 383-410
803 **Bayle V, Arrighi JF, Creff A, Nespoulous C, Vialaret J, Rossignol M, Gonzalez E, Paz-Ares J,**
804 **Nussaume L** (2011) Arabidopsis thaliana high-affinity phosphate transporters exhibit
805 multiple levels of posttranslational regulation. The Plant Cel **23:** 1523-1535
806 **Bi X, Corpina, R. A., & Goldberg, J.** (2002) Structure of the Sec23/24-Sar1 pre-budding complex
807 of the COPII vesicle coat. Nature **419:** 271-277
808 **Bisnett BJ, Condon BM, Lamb CH, Georgiou GR, Boyce M** (2020) Export Control: Post-
809 transcriptional Regulation of the COPII Trafficking Pathway. Front Cell Dev Biol **8:**
810 618652
811 **Bolte S, Cordelieres FP** (2006) A guided tour into subcellular colocalization analysis in light
812 microscopy. J Microsc **224:** 213-232
813 **Cabantous S, Nguyen HB, Pedelacq JD, Koraichi F, Chaudhary A, Ganguly K, Lockard MA,**
814 **Favre G, Terwilliger TC, Waldo GS** (2013) A new protein-protein interaction sensor
815 based on tripartite split-GFP association. Scientific reports **3:** 2854
816 **Chiu CY, Tsai, C. D., Wang, J. Y., Tsai, M. H., McGinness, A. J., Lung, H. F., Kanno, S.,**
817 **Kriechbaumer, V. & Liu, T. Y.** (2024) Phosphate starvation-induced CORNICHON
818 HOMOLOG 5 as endoplasmic reticulum cargo receptor for PHT1 transporters in
819 Arabidopsis. bioRxiv**:** 2024.2006.2020.599911
820 **Chung KP, Zeng Y, Jiang L** (2016) COPII paralogs in plants: functional redundancy or diversity?
821 Trends in Plant Science **21:** 758-769
822 **d'Enfert C, Wuestehube, L. J., Lila, T., & Schekman, R.** (1991) Sec12p-dependent membrane
823 binding of the small GTP-binding protein Sar1p promotes formation of transport
824 vesicels from the ER. The Journal of cell biology **114:** 663-670
825 **daSilva LL, Snapp EL, Denecke J, Lippincott-Schwartz J, Hawes C, Brandizzi F** (2004)
826 Endoplasmic reticulum export sites and Golgi bodies behave as single mobile secretory
827 units in plant cells. The Plant Cell **16:** 1753-1771
828 **Dharmasiri S, Swarup, R., Mockaitis, K., Dharmasiri, N., Singh, S. K., Kowalchyk, M., ... &**
829 **Estelle, M.** (2006) AXR4 is required for localization of the auxin influx facilitator AUX1.
830 Science **312:** 1218-1220
831 **Gimeno RE, Espenshade, P., & Kaiser, C. A.** (1995) SED4 encodes a yeast endoplasmic
832 reticulum protein that binds Sec16p and participates in vesicle formation. The Journal
833 of cell biology **131:** 325-338
834 **González E, Solano R, Rubio V, Leyva A, Paz-Ares J** (2005) PHOSPHATE TRANSPORTER TRAFFIC
835 FACILITATOR1 is a plant-specific SEC12-related protein that enables the endoplasmic
836 reticulum exit of a high-affinity phosphate transporter in Arabidopsis. The Plant Cell **17:**
837 3500-3512

838 **Hanton SL, Chatre L, Matheson LA, Rossi M, Held MA, Brandizzi F** (2008) Plant Sar1 isoforms
839 with near-identical protein sequences exhibit different localisations and effects on
840 secretion. Plant Molecular Biology **67:** 283-294
841 **Hanton SL, Chatre L, Renna L, Matheson LA, Brandizzi F** (2007) De novo formation of plant
842 endoplasmic reticulum export sites is membrane cargo induced and signal mediated.
843 Plant Physiology **143:** 1640-1650
844 **Hanton SL, Matheson LA, Chatre L, Brandizzi F** (2009) Dynamic organization of COPII coat
845 proteins at endoplasmic reticulum export sites in plant cells. The Plant Journal **57:** 963-
846 974
847 **Huang TK, Han CL, Lin SI, Chen YJ, Tsai YC, Chen YR, Chen JW, Lin WY, Chen PM, Liu TY, Chen**
848 **YS, Sun CM, Chiou TJ** (2013) Identification of downstream components of ubiquitin-
849 conjugating enzyme PHOSPHATE2 by quantitative membrane proteomics in
850 Arabidopsis roots. The Plant Cell **25:** 4044-4060
851 **Joiner AMN, Fromme JC** (2021) Structural basis for the initiation of COPII vesicle biogenesis.
852 Structure **29:** 859-872 e856
853 **Kim DI, Birendra KC, Zhu W, Motamedchaboki K, Doye V, Roux KJ** (2014) Probing nuclear pore
854 complex architecture with proximity-dependent biotinylation. Proc Natl Acad Sci U S A
855 **111:** E2453-2461
856 **Kodera C, Yorimitsu T, Nakano A, Sato K** (2011) Sed4p stimulates Sar1p GTP hydrolysis and
857 promotes limited coat disassembly. Traffic **12:** 591-599
858 **Kota J, Gilstring CF, Ljungdahl PO** (2007) Membrane chaperone Shr3 assists in folding amino
859 acid permeases preventing precocious ERAD. J Cell Biol **176:** 617-628
860 **Kota J, Ljungdahl PO** (2005) Specialized membrane-localized chaperones prevent aggregation
861 of polytopic proteins in the ER. The Journal of cell biology **168:** 79-88
862 **Kurokawa K, Nakano A** (2019) The ER exit sites are specialized ER zones for the transport of
863 cargo proteins from the ER to the Golgi apparatus. The journal of biochemistry **165:**
864 109-114
865 **Lau WTW, Howson, R. W., Malkus, P., Schekman, R., & O'Shea, E. K.** (2000) Pho86p, an
866 endoplasmic reticulum (ER) resident protein in Saccharomyces cerevisiae, is required
867 for ER exit of the high-affinity phosphate transporter Pho84p. Proceedings of the
868 National Academy of Sciences **97:** 1107-1112
869 **Li B, Zeng, Y., Cao, W., Zhang, W., Cheng, L., Yin, H., ... & Jiang, L.** (2021) A distinct giant coat
870 protein complex II vesicle population in Arabidopsis thaliana. Nature Plants **7:** 1335-
871 1346
872 **Liang X, Li SW, Gong LM, Li S, Zhang Y** (2020) COPII components Sar1b and Sar1c play distinct
873 yet interchangeable roles in pollen development. Plant Physiology **183:** 974-985

874 **Liu TY, Chou WC, Chen WY, Chu CY, Dai CY, Wu PY** (2018) Detection of membrane protein-
875 protein interaction in planta based on dual-intein-coupled tripartite split-GFP
876 association. The Plant Journal **94:** 426-438
877 **Liu TY, Huang TK, Tseng CY, Lai YS, Lin SI, Lin WY, Chen JW, Chiou TJ** (2012) PHO2-dependent
878 degradation of PHO1 modulates phosphate homeostasis in Arabidopsis. Plant Cell **24:**
879 2168-2183
880 **Liu TY, Huang TK, Yang SY, Hong YT, Huang SM, Wang FN, Chiang SF, Tsai SY, Lu WC, Chiou TJ**
881 (2016) Identification of plant vacuolar transporters mediating phosphate storage.
882 Nature communications **7:** 11095
883 **Liu TY, Tsai, M. H., Wang, J. Y.,, Lung HF, Chiu CY, Chow HX, Lu CA** (2025) CORNICHON
884 HOMOLOG 5-dependent ER export of membrane cargoes in phosphate-starved
885 Arabidopsis root as revealed by membrane proteomic analysis. bioRxiv**:**
886 2024.2012.2030.630708
887 **Lupanga U, Rohrich R, Askani J, Hilmer S, Kiefer C, Krebs M, Kanazawa T, Ueda T, Schumacher**
888 **K** (2020) The Arabidopsis V-ATPase is localized to the TGN/EE via a seed plant-specific
889 motif. Elife **9**
890 **Mair A, Xu SL, Branon TC, Ting AY, Bergmann DC** (2019) Proximity labeling of protein
891 complexes and cell-type-specific organellar proteomes in Arabidopsis enabled by
892 TurboID. elife **8**
893 **McMahon C, Studer SM, Clendinen C, Dann GP, Jeffrey PD, Hughson FM** (2012) The structure
894 of Sec12 implicates potassium ion coordination in Sar1 activation. Journal of Biological
895 Chemistry **287:** 43599-43606
896 **Miller E, Antonny, B., Hamamoto, S., & Schekman, R.** (2002) Cargo selection into COPII
897 vesicles is driven by the Sec24p subunit. The EMBO journal**:** 6105-6113
898 **Millner PD, & Kitt, D. G.** (1992) The Beltsville method for soilless production of vesicular-
899 arbuscular mycorrhizal fungi. Mycorrhiza **2:** 9-15
900 **Montegna EA, Bhave M, Liu Y, Bhattacharyya D, Glick BS** (2012) Sec12 binds to Sec16 at
901 transitional ER sites. PLoS One **7:** e31156
902 **Nussaume L, Kanno S, Javot H, Marin E, Pochon N, Ayadi A, Nakanishi TM, Thibaud MC** (2011)
903 Phosphate import in plants: focus on the PHT1 transporters. Frontiers in plant science
904 **2:** 83
905 **Paul S, Audhya A, Cui Q** (2023) Molecular mechanism of GTP binding-and dimerization-
906 induced enhancement of Sar1-mediated membrane remodeling. Proceedings of the
907 National Academy of Sciences **120:** e2212513120
908 **Saito-Nakano Y, Nakano A** (2000) Sed4p functions as a positive regulator of Sar1p probably
909 through inhibition of the GTPase activation by Sec23p. Genes to Cells **5:** 1039-1048

910 **Saito K, Yamashiro K, Shimazu N, Tanabe T, Kontani K, Katada T** (2014) Concentration of Sec12
911 at ER exit sites via interaction with cTAGE5 is required for collagen export. Journal of
912 Cell Biology **206:** 751-762
913 **Schlücking K, Edel KH, Koster P, Drerup MM, Eckert C, Steinhorst L, Waadt R, Batistic O, Kudla**
914 **J** (2013) A new β-estradiol-inducible vector set that facilitates easy construction and
915 efficient expression of transgenes reveals CBL3-dependent cytoplasm to tonoplast
916 translocation of CIPK5. Mol Plant **6:** 1814-1829
917 **Schneider CA, Rasband WS, Eliceiri KW** (2012) NIH Image to ImageJ: 25 years of image analysis.
918 Nature methods **9:** 671-675
919 **Shen J, Yuan, L., Zhang, J., Li, H., Bai, Z., Chen, X., ... & Zhang, F.** (2011) Phosphorus dynamics:
920 from soil to plant. Plant physiology **156:** 997-1005
921 **Spitzer M, Wildenhain J, Rappsilber J, Tyers M** (2014) BoxPlotR: a web tool for generation of
922 box plots. Nature methods **11:** 121-122
923 **Stagg SM, Gurkan C, Fowler DM, LaPointe P, Foss TR, Potter CS, Carragher B, Balch WE** (2006)
924 Structure of the Sec13/31 COPII coat cage. Nature **439:** 234-238
925 **Supek F, Madden DT, Hamamoto S, Orci L, Schekman R** (2002) Sec16p potentiates the action
926 of COPII proteins to bud transport vesicles. The Journal of cell biology **158:** 1029-1038
927 **Takagi J, Kimori Y, Shimada T, Hara-Nishimura I** (2020) Dynamic Capture and Release of
928 Endoplasmic Reticulum Exit Sites by Golgi Stacks in Arabidopsis. iScience **23:** 101265
929 **Takagi J, Renna L, Takahashi H, Koumoto Y, Tamura K, Stefano G, Fukao Y, Kondo M,**
930 **Nishimura M, Shimada T, Brandizzi F, Hara-Nishimura I** (2013) MAIGO5 functions in
931 protein export from Golgi-associated endoplasmic reticulum exit sites in Arabidopsis.
932 The Plant Cell **25:** 4658-4675
933 **Takeuchi M, Ueda, T., Sato, K., Abe, H., Nagata, T., & Nakano, A.** (2000) A dominant negative
934 mutant of Sar1 GTPase inhibits protein transport from the ER to the Golgi apparatus in
935 tobacco and Arabidopsis cultured cells. The Plant Journal **23:** 517-525
936 **Tang BL, Wang Y, Ong YS, Hong W** (2005) COPII and exit from the endoplasmic reticulum.
937 Biochim Biophys Acta **1744:** 293-303
938 **Tidy A, Abu Bakar N, Carrier D, Kerr ID, Hodgman C, Bennett MJ, Swarup R** (2024) Mechanistic
939 insight into the role of AUXIN RESISTANCE4 in trafficking of AUXIN1 and LIKE AUX1-2.
940 Plant Physiology **194:** 422-433
941 **Van der Verren SE, Zanetti G** (2023) The small GTPase Sar1, control centre of COPII trafficking.
942 FEBS letters **597:** 865-882
943 **Wang X, Xu M, Gao C, Zeng Y, Cui Y, Shen W, Jiang L** (2020) The roles of endomembrane
944 trafficking in plant abiotic stress responses. Journal of integrative plant biology **62:** 55-
945 69

946 **Wei T, Wang A** (2008) Biogenesis of cytoplasmic membranous vesicles for plant potyvirus
947 replication occurs at endoplasmic reticulum exit sites in a COPI-and COPII-dependent
948 manner. Journal of virology **82:** 12252-12264
949 **Weigel AV, Chang CL, Shtengel G, Xu CS, Hoffman DP, Freeman M, Iyer N, Aaron J, Khuon S,**
950 **Bogovic J, Qiu W, Hess HF, Lippincott-Schwartz J** (2021) ER-to-Golgi protein delivery
951 through an interwoven, tubular network extending from ER. Cell **184:** 2412-2429 e2416
952 **Weissman JT, Plutner H, Balch WE** (2001) The mammalian guanine nucleotide exchange factor
953 mSec12 is essential for activation of the Sar1 GTPase directing endoplasmic reticulum
954 export. Traffic **2:** 465-475
955 **Xu SL, Shrestha R, Karunadasa SS, Xie PQ** (2023) Proximity labeling in plants. Annual review
956 of plant biology **74:** 285-312
957 **Yang YD, Elamawi R, Bubeck J, Pepperkok R, Ritzenthaler C, Robinson DG** (2005) Dynamics of
958 COPII vesicles and the Golgi apparatus in cultured Nicotiana tabacum BY-2 cells
959 provides evidence for transient association of Golgi stacks with endoplasmic reticulum
960 exit sites. Plant Cell **17:** 1513-1531
961 **Yoshimoto K, Hanaoka H, Sato S, Kato T, Tabata S, Noda T, Ohsumi Y** (2004) Processing of
962 ATG8s, ubiquitin-like proteins, and their deconjugation by ATG4s are essential for plant
963 autophagy. The Plant Cell **16:** 2967-2983
964 **Zeng Y, Chung KP, Li B, Lai CM, Lam SK, Wang X, Cui Y, Gao C, Luo M, Wong KB, Schekman R,**
965 **Jiang L** (2015) Unique COPII component AtSar1a/AtSec23a pair is required for the
966 distinct function of protein ER export in Arabidopsis thaliana. Proceedings of the
967 National Academy of Sciences **112:** 14360-14365
968 **Zeuschner D, Geerts WJ, van Donselaar E, Humbel BM, Slot JW, Koster AJ, Klumperman J**
969 (2006) Immuno-electron tomography of ER exit sites reveals the existence of free
970 COPII-coated transport carriers. Nat Cell Biol **8:** 377-383
971 **Zhang Z, Nakamura S, Yamasaki A, Uehara M, Takemura S, Tsuchida K, Kamiya T, Shigenobu**
972 **S, Yamaguchi K, Fujiwara T, Ishiguro S, Takano J** (2024) Arabidopsis KNS3 and its two
973 homologs mediate endoplasmic reticulum-to-plasma membrane traffic of boric acid
974 channels. Journal of Experimental Botany **75:** 7046-7065
975

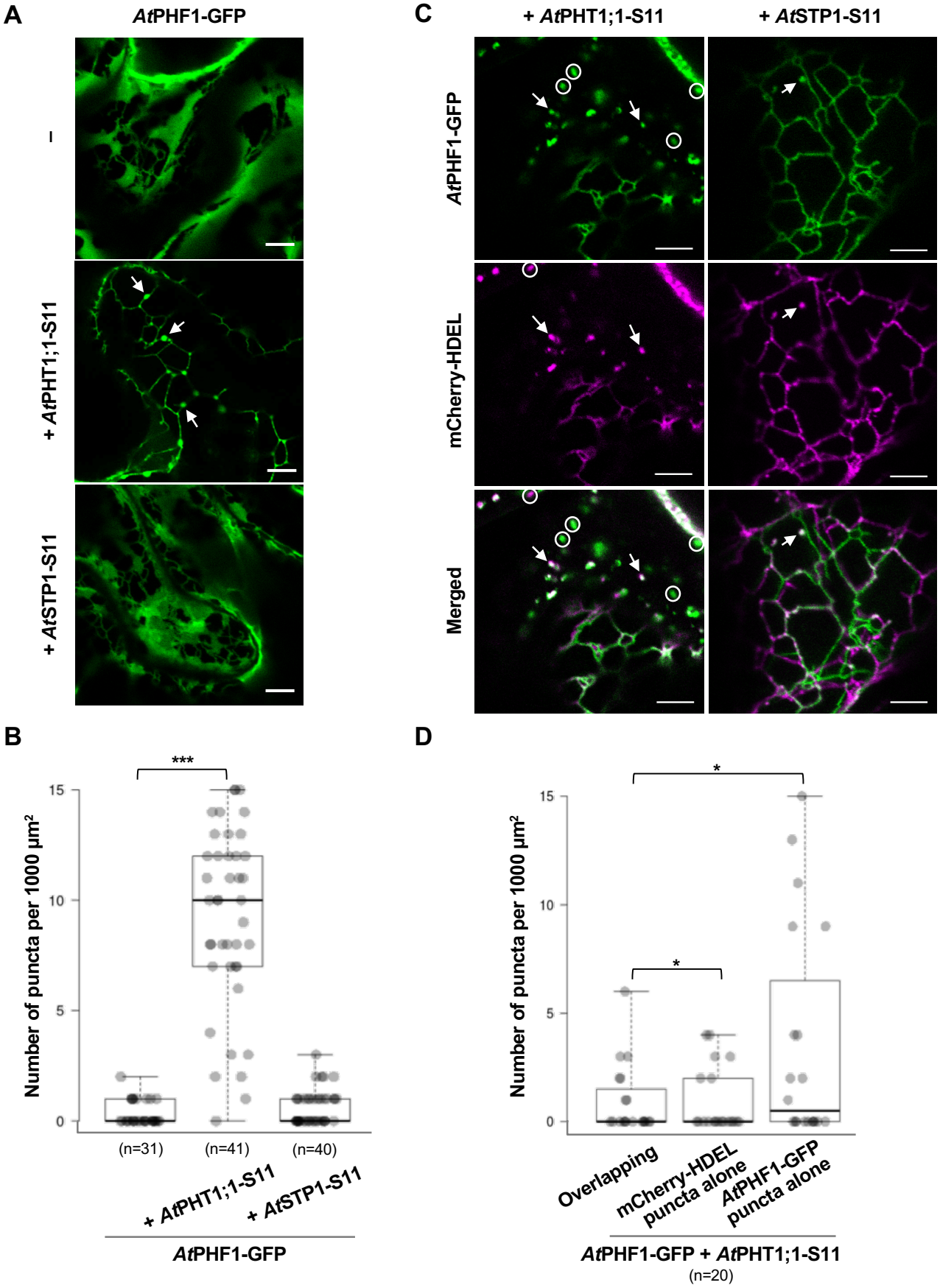
A
AtPHF1-GFP
–
+ AtPHT1;1-S11
+ AtSTP1-S11
C
+ AtPHT1;1-S11
+ AtSTP1-S11
AtPHF1-GFP
mCherry-HDEL
Merged
B
***
Number of puncta per 1000 µm²
15
10
5
0
(n=31)
(n=41)
(n=40)
+ AtPHT1;1-S11
+ AtSTP1-S11
AtPHF1-GFP
D
*
*
Number of puncta per 1000 µm²
15
10
5
0
Overlapping
mCherry-HDEL puncta alone
AtPHF1-GFP puncta alone
AtPHF1-GFP + AtPHT1;1-S11
(n=20)

Figure 1. *At*PHT1;1 overexpression triggers partial distribution of *At*PHF1 to punctate structures in agro-infiltrated *N. benthamiana* leaves. **(A)** Distribution of *At*PHF1-GFP in the absence or presence of *At*PHT1;1-S11 or *At*STP1-S11 co-expression. Arrows, punctate structures. **(B)** Quantification analysis of (**A**) from three independent experiments. **(C)** Co-localization analysis of *At*PHF1-GFP puncta and mCherry-HDEL puncta in the presence of *At*PHT1;1-S11 or *At*STP1-S11 co-expression. Arrows, overlapping puncta; circles, non-overlapping puncta. **(D)** The quantification of (**C**) from three independent experiments. Representative confocal images at the peripheral layers of the epidermis are shown in (**A**) and (**C**); scale bars, 5 µm. Box plots show medians (center lines), interquartile ranges (boxes), data ranges (whiskers), and data points (dots) in (**B**) and (**D**). The number of regions of interest used for quantification is shown in parentheses. ***, $P < 0.001$ versus *At*PHF1-GFP expression alone in (**B**); *, $P < 0.05$ versus overlapping puncta in (**D**); Dunnett's test for multiple comparisons.

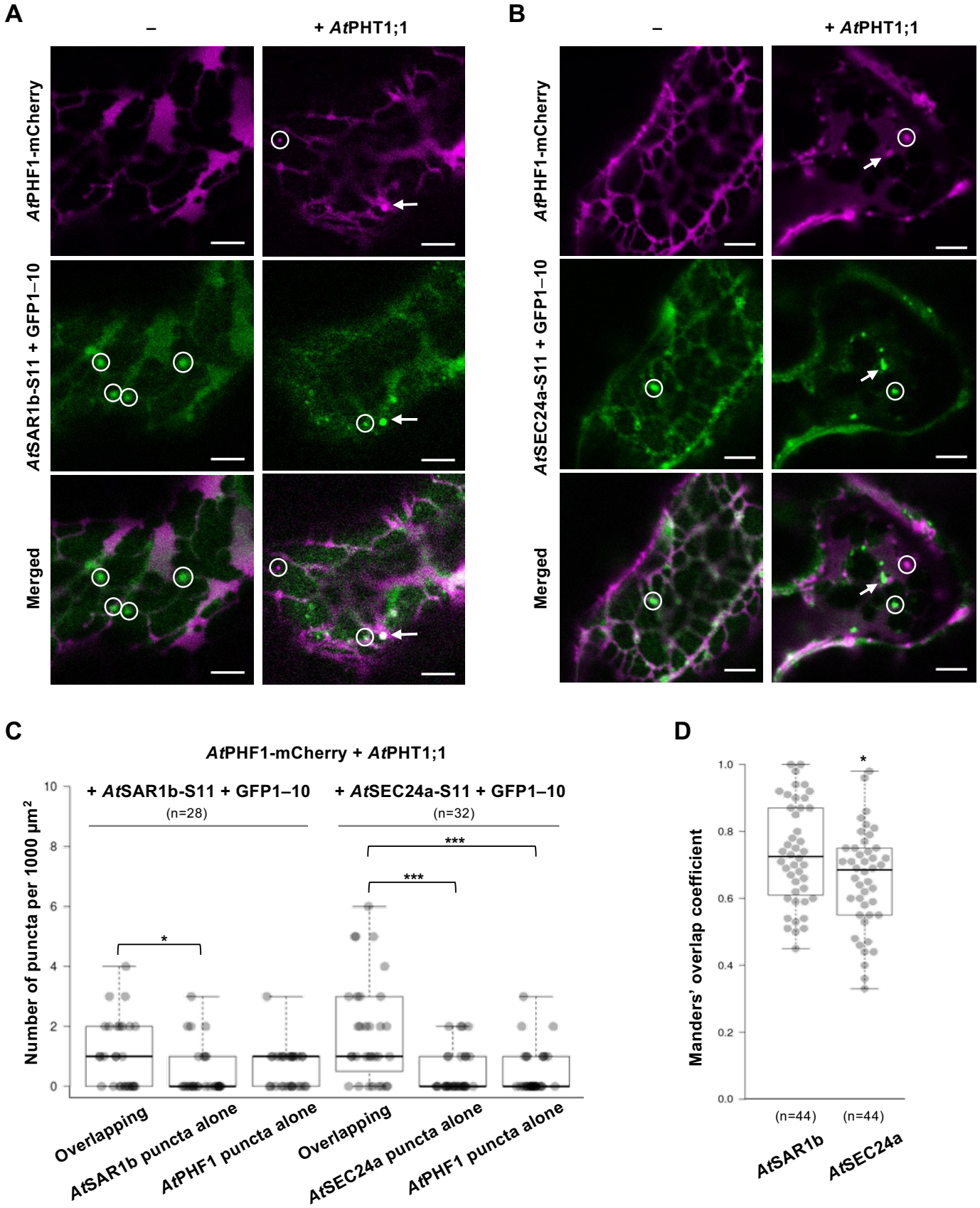
A
–
+ AtPHT1;1
AtPHF1-mCherry
AtSAR1b-S11 + GFP1–10
Merged
B
–
+ AtPHT1;1
AtPHF1-mCherry
AtSEC24a-S11 + GFP1–10
Merged
C
AtPHF1-mCherry + AtPHT1;1
+ AtSAR1b-S11 + GFP1–10
(n=28)
+ AtSEC24a-S11 + GFP1–10
(n=32)
Number of puncta per 1000 µm²
Overlapping
AtSAR1b puncta alone
AtPHF1 puncta alone
Overlapping
AtSEC24a puncta alone
AtPHF1 puncta alone
D
Manders' overlap coefficient
(n=44)
(n=44)
AtSAR1b
AtSEC24a

Figure 2. *At*PHT1;1-induced *At*PHF1 puncta partially co-localize with the ERES markers in agro-infiltrated *N. benthamiana* leaves. (A, **B)** Co-localization of *At*SAR1b-S11 (**A**) and *At*SEC24a-S11 (**B**) with *At*PHF1-mCherry in the absence or presence of *At*PHT1;1 overexpression. Representative confocal images were taken at the peripheral layer of the epidermis. Arrows, overlapping puncta; circles, non-overlapping puncta. Scale bars, 5 µm. **(C)** Quantification of co-localization in (**A**) and (**B**). The number of regions of interest used for quantification is shown in parentheses. *, $P < 0.05$; ***, $P < 0.001$; Dunnett's test for multiple comparisons against overlapping with *At*SAR1b or *At*SEC24a. **(D)** Comparison of Manders' overlap coefficient between the co-localization of *At*PHF1-mCherry with *At*SAR1b-S11 and *At*SEC24a-S11. Data were collected from three independent experiments. Box plots show medians (center lines), interquartile ranges (boxes), data ranges (whiskers), and data points (dots). The puncta numbers used for the quantification analysis are shown in parentheses. *, $P < 0.05$; two-tailed Mann-Whitney U test.

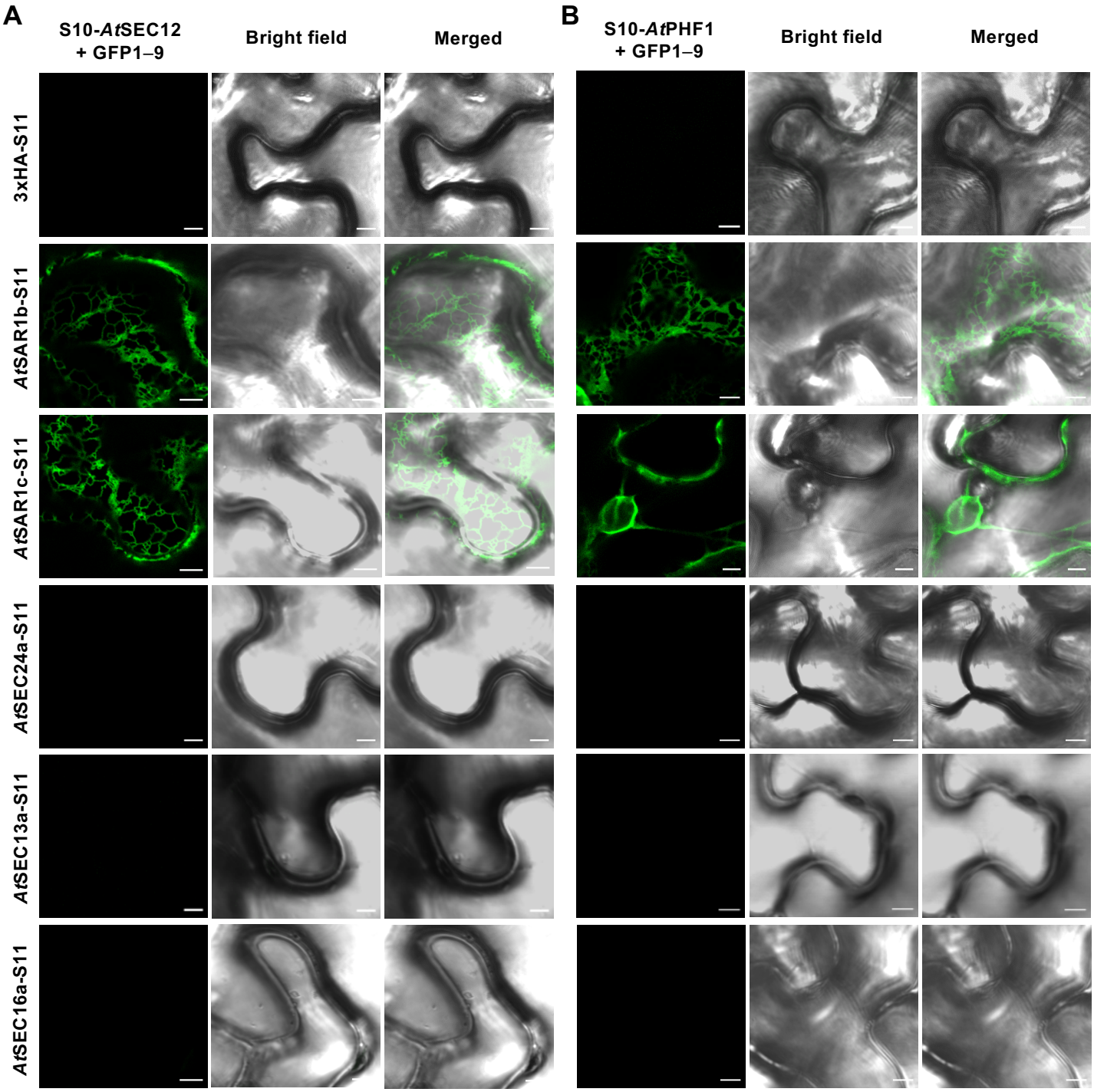

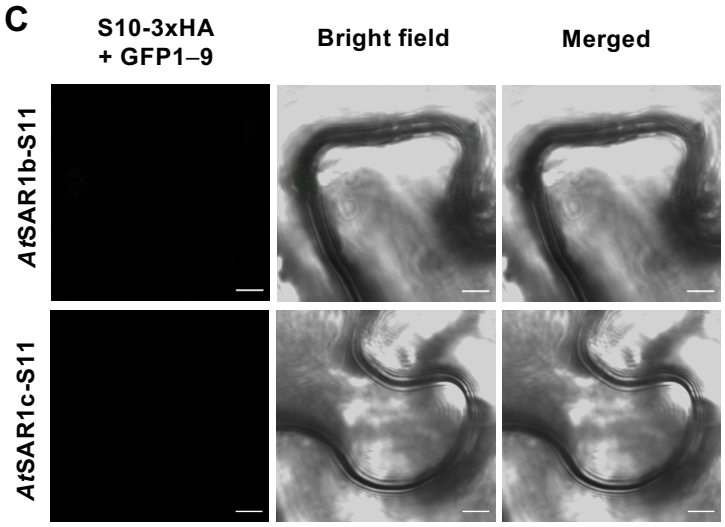

Figure 3. *At*PHF1 interacts with *At*SAR1b and *At*SAR1c *in planta* based on the tripartite split-GFP association in agro-infiltrated *N. benthamiana* leaves. The interaction of S10-*At*SEC12 **(A)** or S10-*At*PHF1 **(B)** with the COPII-related components, *At*SAR1b-, *At*SAR1c-, *At*SEC24a-, *At*SEC13a-, and *At*SEC16a-S11. The interactions with 3xHA-S11 in (**A**) and (**B**) and S10-3xHA (**C**) were used as negative controls. Scale bars, 5 µm. Representative confocal images taken at the peripheral layer of the epidermis are shown from three independent experiments.

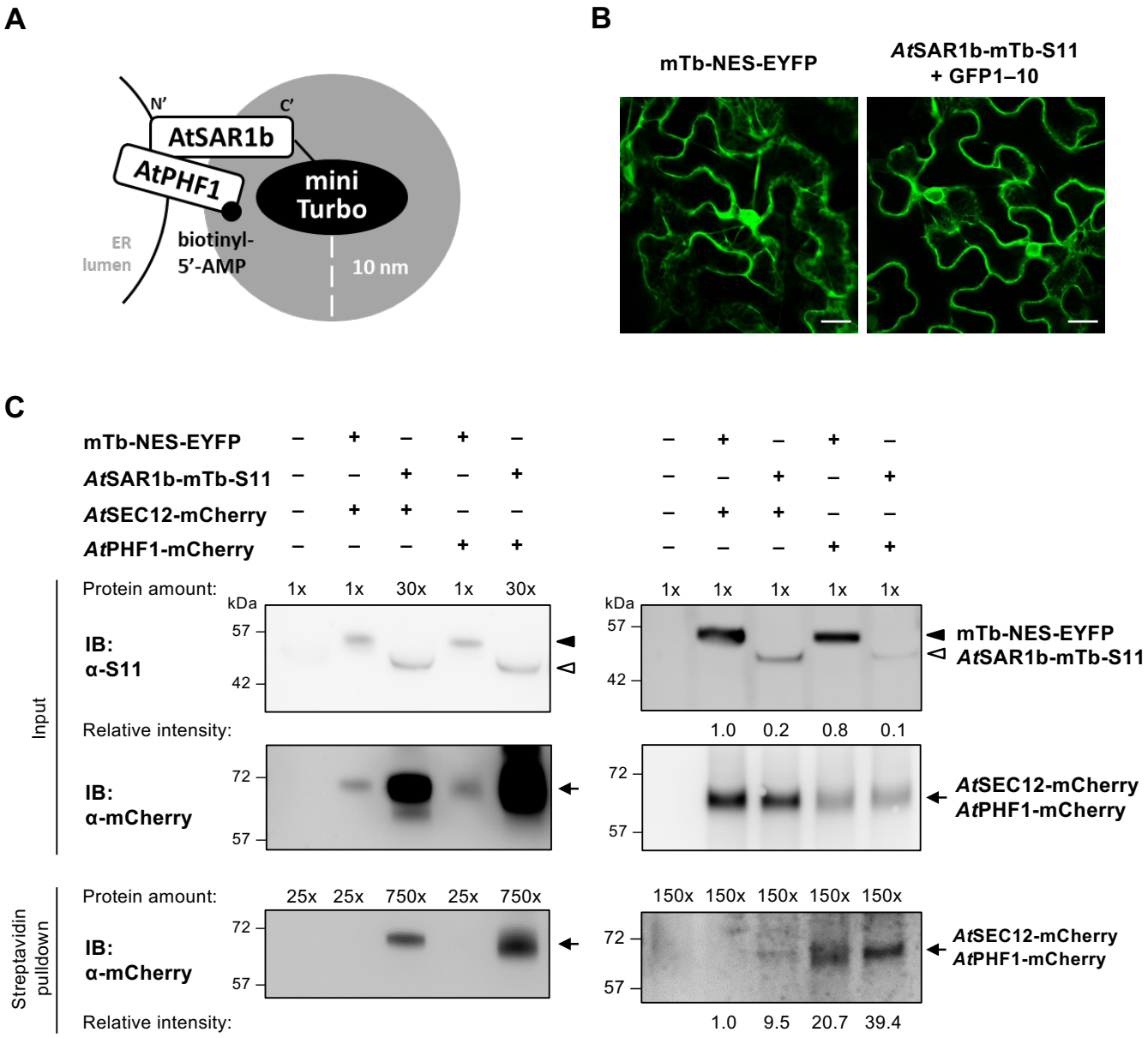

Figure 4. *At*PHF1 interacts with *At*SAR1b *in planta* based on the proximity labeling in agro-infiltrated *N. benthamiana* leaves. (A) Schematic diagrams of mTb-fused bait protein in the proximity of the prey protein. The reactive intermediate biotinyl-5'-AMP biotinylates proximal prey proteins within the indicated range (grey zone). **(B)** The expression and subcellular distribution of mTb-NES-EYFP and *At*SAR1b-mTb-S11. Scale bars, 20 µm. Representative confocal images are shown from three independent experiments. **(C)** The interaction analyses of *At*PHF1-mCherry and *At*SAR1b by proximity labeling. In the left panel, thirty-fold more protein extract expressing *At*SAR1b-mTb-S11 was used as input for Streptavidin pulldown relative to that expressing mTb-NES-EYFP; in the right panel, equal amounts of protein from the samples were used for pulldown. Anti-S11 antibody was used to detect EYFP-tagged and S11-tagged fusion proteins. Representative results are shown from two independent experiments.

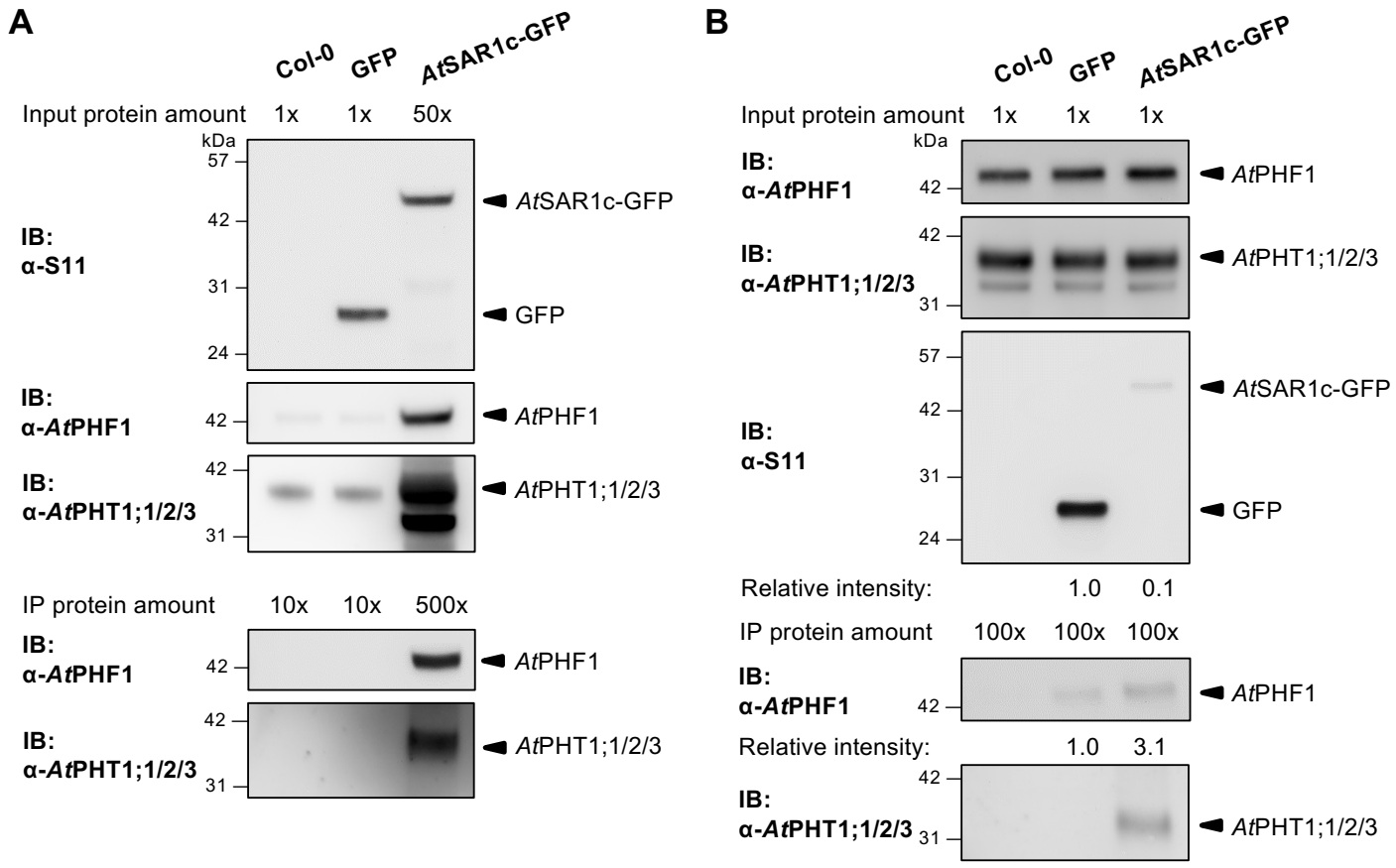

Figure 5. Co-immunoprecipitation of the endogenous *At*PHF1 and *At*PHT1;1/2/3 with *At*SAR1c-GFP in *Arabidopsis* transgenic plants. (A, B) The interaction analyses of *At*SAR1c-GFP with the endogenous *At*PHF1 and *At*PHT1;1/2/3 in 11-day-old wild-type (Col-0), *UBQ10:*GFP, and *UBQ10:At*SAR1c-GFP seedlings subjected to Pi deprivation (0 μM KH_2PO_4, 7 days of starvation). Fifty-fold more protein extract expressing *At*SAR1c-GFP was used as input for GFP-Trap co-immunoprecipitation relative to that expressing free GFP in (**A**). Equal amounts of protein from the samples were used for co-immunoprecipitation in (**B**). Anti-S11 antibody was used to detect GFP fusion proteins. Representative results are shown from three independent experiments.

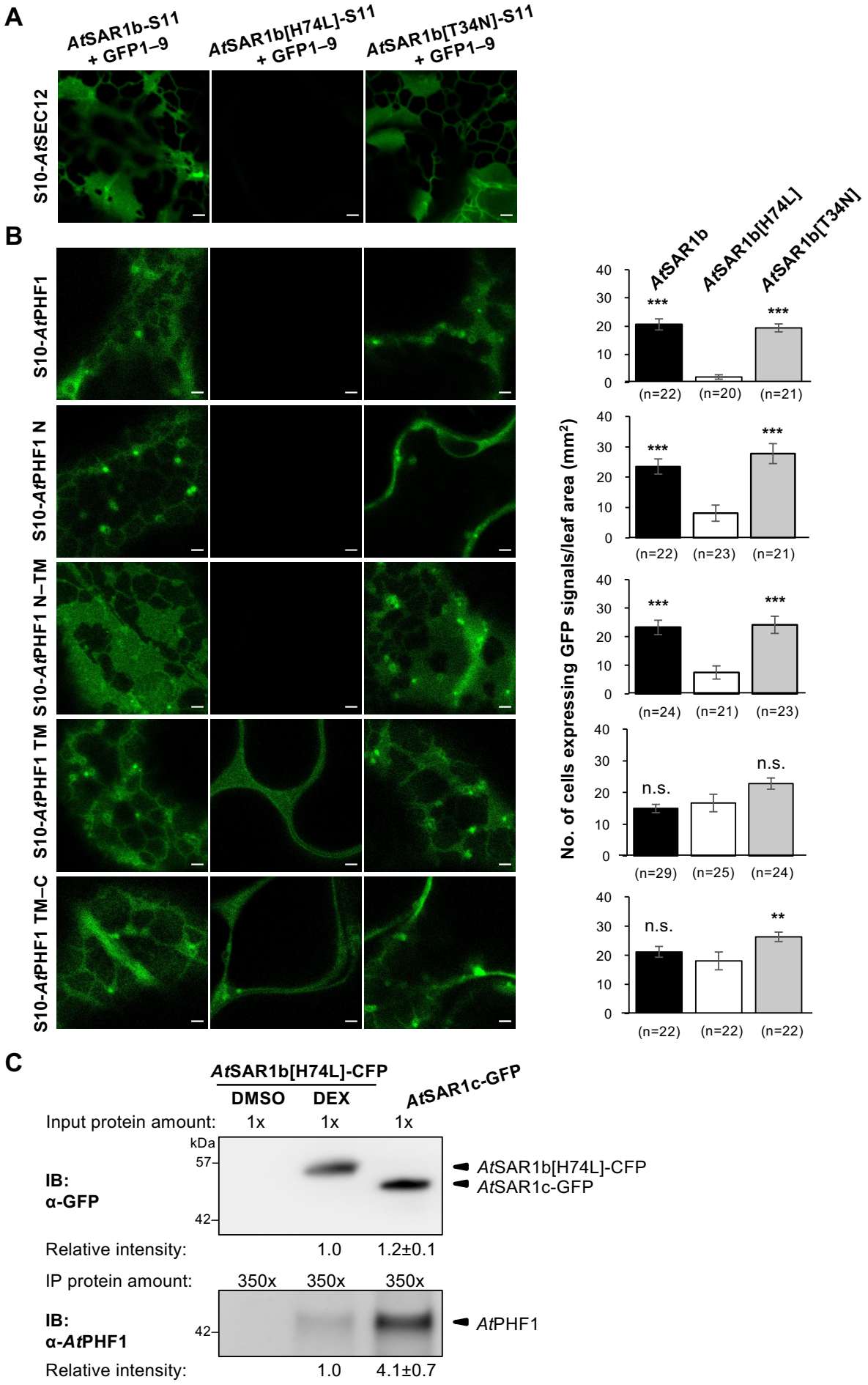
A
AtSAR1b-S11 + GFP1–9
AtSAR1b[H74L]-S11 + GFP1–9
AtSAR1b[T34N]-S11 + GFP1–9
S10-AtSEC12
B
S10-AtPHF1
S10-AtPHF1 N
S10-AtPHF1 N–TM
S10-AtPHF1 TM
S10-AtPHF1 TM–C
AtSAR1b
AtSAR1b[H74L]
AtSAR1b[T34N]
No. of cells expressing GFP signals/leaf area (mm²)
***
n.s.
**
(n=22) (n=20) (n=21)
(n=22) (n=23) (n=21)
(n=24) (n=21) (n=23)
(n=29) (n=25) (n=24)
(n=22) (n=22) (n=22)
C
AtSAR1b[H74L]-CFP
DMSO
DEX
AtSAR1c-GFP
Input protein amount: 1x 1x 1x
kDa
57
42
IB: α-GFP
AtSAR1b[H74L]-CFP
AtSAR1c-GFP
Relative intensity: 1.0 1.2±0.1
IP protein amount: 350x 350x 350x
IB: α-AtPHF1
AtPHF1
Relative intensity: 1.0 4.1±0.7

Figure 6. *At*PHF1 preferentially interacts with the GDP-locked form of *At*SAR1b in agro-infiltrated *N. benthamiana* leaves and *Arabidopsis* transgenic plants. (A, B) The interaction analyses of S10-*At*SEC12 (**A**) and S10-*At*PHF1 variants (**B**) with *At*SAR1b/[H74L]/[T34N]-S11 in agro-infiltrated tobacco leaves. Representative confocal images were taken at the peripheral layer of the epidermis. Scale bars, 2 µm. Quantification indicates the number of cells expressing GFP signals per unit leaf area (mm^2). Data were collected from three independent experiments; the number of confocal images (0.32 x 0.32 mm^2) used for quantification is shown in parentheses. **, $P < 0.01$; ***, $P < 0.001$; Dunnett's test for multiple comparisons against *At*SAR1b[H74L]. Not significant, n.s.. **(C)** Interaction analyses of the WT or GTP-locked form of *At*SAR1 with the endogenous *At*PHF1 were performed in 11-day-old *UBQ10:At*SAR1c-GFP and *dex:At*SAR1b[H74L]-CFP seedlings subjected to Pi deprivation (0 µM KH_2PO_4, 7 days). *dex:At*SAR1b[H74L]-CFP seedlings were treated with 24 hours of 10 µM dexamethasone (DEX) or DMSO. The protein amounts as input for GFP-Trap co-immunoprecipitation are as indicated above the image. An anti-GFP antibody was used to detect GFP and CFP fusion proteins. The relative intensity is shown as mean ± SE from two independent experiments.

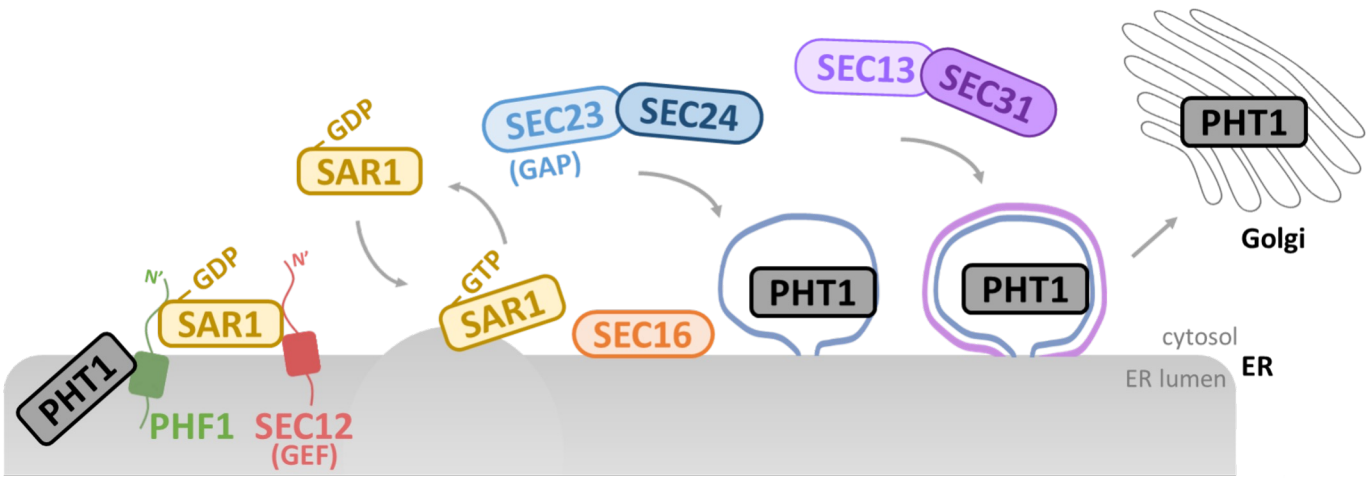

Figure 7. Hypothetical model depicting a role for *At*PHF1 in COPII recruitment for the ER export of *At*PHT1 transporters. The GEF SEC12 recruits and activates SAR1 GTPase by exchanging GDP for GTP. The direct interaction of GTP-bound SAR1 with SEC23 recruits SEC23/24 to form the inner coat, followed by SEC13/31 recruitment to form the outer coat. The ER-resident PHF1 concentrates on ERES triggered by increased PHT1 proteins and interacts with GDP-bound SAR1. While the scaffold protein SEC16 at ERES does not interact with PHF1, the interaction of PHF1 and SAR1 may link to the regulation of SAR1 GTPase recruitment, thereby facilitating COPII assembly at ERES for the ER-to-Golgi transport of PHT1 proteins in the budding COPII vesicles.